International Journal of Fatigue 181 (2024) 108120

Contents lists available at ScienceDirect

International Journal of Fatigue

journal homepage: www.elsevier.com/locate/ijfatigue

Modelling of the surface morphology and size effects on fatigue strength of L-PBF Inconel 718 by comparing different testing specimens

Giuseppe Macoretta [a], Lorenzo Romanelli [a,*], Ciro Santus [a], Luca Romoli [a], Adrian Hugh Alexander Lutey [b], Federico Uriati [b], Gianni Nicoletto [b], Sunil Raghavendra [c], Matteo Benedetti [c], Bernardo Disma Monelli [a]

[a] DICI, Department of Civil and Industrial Engineering, University of Pisa, Largo Lucio Lazzarino 1 56122, Pisa, Italy
[b] DIA, Department of Engineering and Architecture, University of Parma, Parco Area delle Scienze 181/A 43124, Parma, Italy
[c] DII, Department of Industrial Engineering, University of Trento, Via Sommarive 9 38123, Trento, Italy

ARTICLE INFO

Keywords:
Laser-powder bed fusion
High cycle fatigue
Murakami formula
Surface roughness
Highly stressed surface

ABSTRACT

The aim of this study was to investigate the impact of surface roughness and size effect on the uniaxial fatigue strength of aged specimens made of Inconel 718, obtained by laser-powder bed fusion (L-PBF) both under as-built and machined surface conditions. The surface profiles were scanned with a 3D optical profilometer, and then modelled and filtered by the fast Fourier transform. This latter allowed to obtain the relevant parameters to calculate the term $\sqrt{area}$ in the Murakami model to account for the effect of surface roughness on fatigue strength prediction. Two additional terms were added to the standard Murakami formula: one to account for the size effect and the other to consider the nonzero value of the average stress. A cylindrical plain and a miniaturized plain specimens, in the as-built condition, were employed to calibrate the proposed model, while a machined plain cylindrical and a miniaturized notched specimens were used as validators with low prediction errors.

1. Introduction

Additive manufacturing (AM), also known as 3D printing, has revolutionized the manufacturing industry by offering new possibilities in producing complex geometries and custom-designed components. Among the wide range of materials used in metal AM, the Inconel 718 has gained significant attention due to its excellent mechanical properties and high-temperature strength [1]. This metal is a nickel-based superalloy, and its properties make it suitable for critical applications in aerospace, automotive, and energy sectors [2–4]. Despite the usual applications of this alloy at high-temperatures, in Ref. [5] it was recognized that this nickel-based superalloy can also be suitable for components operating at room temperature.

Inconel 718 is especially suited for AM techniques, and one of the prominent methods to be used with this alloy is laser-powder bed fusion (L-PBF) [6,7]. L-PBF involves selectively melting and fusing consecutive layers of metallic powder using a laser beam and resulting in fully dense components if required, or even lattice structures when necessary. The process offers advantages such as reduced material waste, shorter lead times, and the ability to manufacture complex geometries that are otherwise challenging to produce through the traditional manufacturing methods [8].

Despite these benefits offered by the L-PBF technique, in order to achieve the optimal mechanical properties for Inconel 718 parts, a meticulous control of the process parameters and an implementation of post-processing treatments are required [9]. Insufficient control over these parameters can result in defects such as lack of fusion, pores, and keyholes, which introduce significant threats to the mechanical integrity of the final components [10–12]. For this reason, carefully tuning the process parameters is strongly recommended, including laser power, scan velocity, hatch distance, and layer thickness, to ensure the production of defect-free parts with the desired properties and satisfactory productivity. To accomplish this, the identification of a feasible technological parameter region becomes imperative, which is a superimposition of the limits that describe the occurrence of lack of fusion or meltpool instability [13]. The establishment of such a region can be achieved through comprehensive design of experiments approaches [11,14] or the utilization of semi-analytical techniques that leverage the re-elaboration of the Rosenthal solution [15] for a travelling steady-state point heat source [16,17]. By systematically exploring the parameter space within this feasibility region, manufacturers can optimize the L-PBF process and obtain a trade-off between productivity

* Corresponding author.
E-mail address: lorenzo.romanelli@phd.unipi.it (L. Romanelli).

https://doi.org/10.1016/j.ijfatigue.2023.108120
Received 6 October 2023; Received in revised form 28 November 2023; Accepted 22 December 2023
Available online 26 December 2023

Nomenclature

AM	Additive manufacturing
L-PBF	Laser-powder bed fusion
HIP	Hot isostatic pressing
VIGA	Vacuum inert gas and atomization
PSD	Particle size distribution
FFT	Fast Fourier transform
HSS	Highly stressed surface
OM	Optical microscope
OP	Optical profilometer
LEFM	Linear elastic fracture mechanics
P	Laser power
l	Meltpool length
$2r$	Meltpool diameter
A_r	Meltpool aspect ratio
$A_{r,g}$	Grain aspect ratio
B_r	L-PBF build rate
v	Laser scan velocity
h	Hatch distance
t	Layer thickness
a_t	Cutting depth of the turning machining operation
f_t	Feed rate of the turning machining operation
v_t	Cutting speed of the turning machining operation
E_d	Energy density
S_Y	Yield strength
S_U	Ultimate strength
H_V	Vickers hardness
ε_f	Percent elongation at fracture
μ_t	Mean value of the properties obtained from static tensile test
σ_t	Standard deviation of the properties obtained from static tensile test
R	Load ratio of fatigue loading
$\Delta\sigma$	Stress range
σ_a	Amplitude stress
k, b	Basquin parameters
σ_f	Standard deviation of the fatigue data
N	Number of data points of the fatigue curves
$\sigma_{a,i}$	I–th stress amplitude data point
$\hat{\sigma}_{a,i}$	Estimator of the i–th stress amplitude data point
q	Number of parameters of the employed fitting curve
M	Applied bending moment on the miniaturized specimen
W	Bending section modulus
B	Width of the miniaturized specimen minimum cross section
H	Height of the miniaturized specimen minimum cross section
$\sigma_{nom.,max}$	Maximum axial stress in the miniaturized plain specimen according to the beam theory
$\sigma_{real,max}$	Maximum axial stress in the miniaturized plain specimen obtained by FE analyses
C_{mg}	Correction factor for the miniaturized plain specimen geometry
σ_w	Fatigue limit
$\sigma_{pl,fl}$	Fatigue limit of the cylindrical as-built series
$\sigma_{pl,m,fl}$	Fatigue limit of the cylindrical machined series
$\sigma_{mini,fl}$	Fatigue limit of the miniaturized plain as-built series
$\sigma_{mini,n,fl}$	Fatigue limit of the miniaturized notched as-built series
$\sigma_{pl,a}$	Stress amplitude of the cylindrical plain as-built series
$\sigma_{pl,m,a}$	Stress amplitude of the cylindrical plain machined series
$\sigma_{mini,a}$	Stress amplitude of the miniaturized plain as-built series
$\sigma_{mini,n,a}$	Stress amplitude of the miniaturized notched as-built series
S_q	Areal roughness parameter indicating the root mean square of the heights
S_{sk}	Areal Skewness parameter to describe the symmetry of the scanned portion with respect to the mean surface
S_{ku}	Areal Kurtosis parameter to describe the sharpness of the roughness profile
S_p	Areal roughness parameter indicating the maximum peak height
S_v	Areal roughness parameter indicating the maximum valley depth
S_z	Areal roughness parameter indicating the sum of the maximum peak height and maximum valley depth
S_a	Areal roughness parameter indicating the arithmetical mean height
S	Highly stressed surface
S_{pl}	Highly stressed surface of the cylindrical specimen
S_{mini}	Highly stressed surface of the miniaturized plain specimen
$S_{mini,n}$	Highly stressed surface of the miniaturized notched specimen
S_0	Reference surface of the proposed model
m	Exponent of the proposed size effect term
K_I	Mode I stress intensity factor
F	Geometric correction factor of linear elastic fracture mechanics

and metal quality and its strength [18]. The proper adjustment of process parameters mitigates the risks associated with defects, enabling the production of structurally reliable Inconel 718 components with the desired mechanical properties. Furthermore, post-process treatments, such as solubilization and double aging heat treatments, contribute significantly to enhancing the mechanical performance of AM components, particularly for the investigated Inconel 718. These treatments are commonly employed to refine the microstructure, elevate the high-temperature strength, and alleviate residual stresses within the material [12,19,20]. The solubilization treatment involves heating the fabricated components to a specific temperature, followed by rapid quenching, which dissolves the secondary phases and homogenizes the microstructure. Subsequently, the double aging process induces two

$area$	Area of internal defects according to the Murakami formula
p	Pitch distance between two consecutive roughness valleys
a	Crack depth of fracture mechanics readapted to valley depth in the Murakami model
$\sqrt{area_{\mathrm{R}}}$	Murakami roughness parameter
$\sqrt{area_{\mathrm{R,1}}}$	Maximum Murakami roughness parameter of the cylindrical and as-built specimen
$\sqrt{area_{\mathrm{R,2}}}$	Maximum Murakami roughness parameter of the miniaturized plain and as-built specimen
$\sqrt{area_{\mathrm{R,3}}}$	Maximum Murakami roughness parameter of the cylindrical and machined specimen
$\sqrt{area_{\mathrm{R,4}}}$	Maximum Murakami roughness parameter of the miniaturized notched and as-built specimen
$\sqrt{area_{\mathrm{crit}}}$	Critical value of $\sqrt{area}$ for the validity of the Murakami formula

distinct aging steps to the material, and it promotes the precipitation of fine γ'' and γ' phases. These precipitates enhance the strength and the creep resistance of Inconel 718, contributing to its superior static and fatigue properties [21]. Although a careful control of process parameters, internal defects are inevitable. The almost complete elimination of these defects is crucial for ensuring the reliability and performance of critical highly-stressed components. Hot isostatic pressing (HIP) plays a beneficial role in this regard [19,22]. HIP is a post-process treatment that makes the fabricated components to simultaneously experience both high temperature and high pressure, effectively closing internal voids, thus reducing porosity and enhancing the overall density of the material. By eliminating the internal defects, HIP significantly improves the mechanical integrity and fatigue resistance of the AMed Inconel 718 components, making them suitable for those demanding applications where the presence of defects is unacceptable. However, it is important to note that HIP entails supplementary manufacturing costs and process times and hence should not be perceived as a remedy for improperly tuned L-PBF process parameters. On the contrary, it serves as a complementary step to ensure the exceptional quality of the final components.

Considering what stated about the impact of defects on the mechanical behaviour, the fatigue strength of AMed components, also made of Inconel 718, is becoming a widely diffused topic of research in the engineering field [18,23,24]. The fatigue strength of specimens fabricated by traditional technologies has been longly investigated as in Refs. [25–27], and the acquired knowledge is clearly useful to face with the fatigue design of AMed specimens. The surface roughness and internal defects within AMed components have a significant impact on their fatigue strength [28]. Indeed, surface roughness and internal defects, such as pores and lack of fusion, act as stress concentrators and thus reduce the fatigue life [29]. Furthermore, the interaction between surface roughness and internal defects can create synergistic effects that further deteriorate the material's fatigue performance [30], and various models were proposed and employed to account for these effects in fatigue strength predictions.

In Ref. [31] it was highlighted the possibility to use critical plane criteria, such as Fatemi–Socie (FS) and Smith Watson and Topper (SWT), to predict the fatigue strength of AM-produced specimens under multiaxial loadings. The role of the defects was included considering that the constants of the criteria were calculated involving specimens produced in the same conditions of those used as validators. In Ref. [32] the FS multiaxial fatigue criterion was employed to assess the fatigue strength of smooth specimens of Ti–6Al–4V produced by L-PBF and post-processed through HIP, and it was highlighted that the calculated FS parameter was well correlated among the investigated different loadings such as tensile-compression, torsion, axial-torsion in phase and out of phase. Given the recent diffusion of the modified version of the FS multiaxial fatigue criterion proposed by Gates and Fatemi in Ref. [33], this new criterion was employed in Refs. [34,35] to predict the fatigue strength of AMed specimens wrought and as-built made of 17–4 PH and Ti–6Al–4V, respectively. In addition, and as concerns the fatigue strength of AMed notched components, the Theory of Critical Distances is a powerful and recognized tool for fatigue strength predictions. It can be used in its usual (uniaxial) form [36] or combined with multiaxial fatigue criteria [37], and the values of the critical distances can be calculated according to the classical El-Haddad formulation [38] or by combining specimens with different notches severity [39–41]. Some examples of the fatigue strength assessment of AMed specimens, using this technique, were presented in Refs. [41–44].

Alternatively, given the key role of defects in the fatigue behaviour of 3D printed parts, extensive research has been conducted in this field, with a primary focus on integrating damage tolerant approaches into the design of AMed components [45]. An example is provided by fracture mechanics approaches as in Ref. [46] where the classical Paris law was employed to calculate the number of cycles to failure of AMed components, and the effect of the surface roughness was modelled setting the initial crack length of the formula equal to the maximum valley depth of the profile. In Refs. [47,48] a reformulation of the Paris law was proposed to investigate the fatigue performance of notched and plain specimens of Ti–6Al–4V and 17-4PH under various loadings and after different heat treatments. A fatigue crack growth analysis program (FASTRAN) was used, which is based on the plasticity induced crack closure mechanism. In Ref. [49] the generalized Paris law, proposed by Pugno et al. in Ref. [50], was employed to investigate the fatigue behaviour of cylindrical and thin-walled specimens made of Ti–6Al–4V under various loadings. In Ref. [51] the Modes I and II mixed-mode small crack growth was used to predict the fatigue strength of specimens made of Ti–6Al–4V and 17-4 PH under multiaxial loadings.

Finally, many studies employed the well-established $\sqrt{area}$ approach proposed by Murakami in Ref. [52]. Given that it was highlighted the detrimental effect given by the surface roughness, the potential defects near the surface and their synergistic effect [34,53–55], the term $\sqrt{area}$ to use in the Murakami formula can be calculated as the sum of the contribution due to the surface roughness and the internal defects near the surface, as highlighted in Ref. [31]. The effectiveness of these fatigue design tools are only established after a robust experimental validation.

The fatigue testing of L-PBF components presents numerous challenges due to their inherent directional nature and complex surface morphologies [10,22,56]. A recent advancement by Uriati and Nicoletto [57] introduced a novel mini-specimen geometry, which presents two sides, and its fatigue strength can be investigated as that of plain or notched specimens depending on the side which experiences the tensile stress during the test. Unlike conventional specimens, mini specimens cannot necessitate the use of supporting structures, providing a practical solution to investigate the effects of different building orientations on the fatigue performance of L-PBF components [58]. They can offer a simplified evaluation of the material response to fatigue for comparison purposes. However, it is important to note that the sizes of mini specimens pose the necessity to introduce a size effect factor with respect to the classical cylindrical plain specimen.

To provide a comprehensive understanding of the fatigue behaviour including all the issues briefly referenced in this introduction, this paper focuses on investigating the fatigue characteristics of both conventional and mini-specimens of Inconel 718 produced via L-PBF and aged. Moreover, the experimentation encompasses two surface conditions, namely as-built and machined surfaces. The surfaces of the 3D

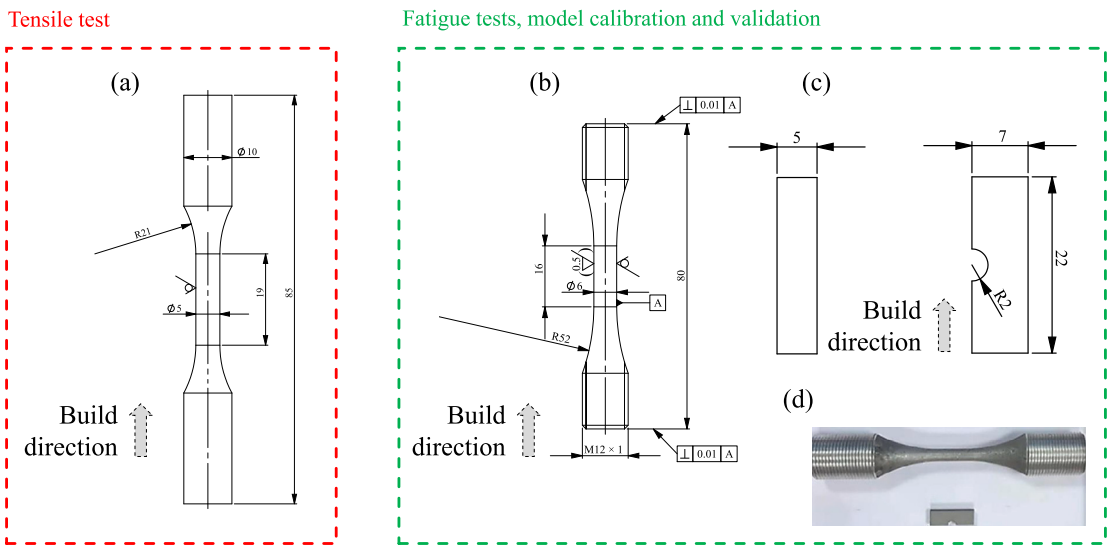

Fig. 1. Geometries and dimensions (in mm) of specimens involved in the research: (a) tensile test specimen, (b) cylindrical plain specimen for fatigue strength assessment and fatigue strength prediction validation, (c) miniaturized specimen for fatigue strength assessment and fatigue strength prediction validation and (d) image to highlight the different sizes between the cylindrical and the miniaturized specimens.

printed specimens were analysed through a 3D optical profilometer (OP), which is an efficient tool for analysing the surface profiles of fractured and untested specimens in order to investigate the structural properties of the materials, as shown in Refs. [24,37,59–63]. An extension of the Murakami formula [52,64], after modelling the observed surface profiles through the sum of harmonics, was proposed for fatigue strength predictions including the effects of surface roughness, nonzero average stress and the different sizes of the specimens. The parameters of the proposed formula were tuned by combining the conventional cylindrical plain and the miniaturized plain specimens in the as-built condition, while the cylindrical plain specimen, after machining operation by turning, and the as-built miniaturized notched specimen were employed to validate the proposed procedure.

2. Materials and methods

2.1. Specimen manufacturing and geometries

The Inconel 718 powder, supplied by Heareus Electro-Nite Gmbh & Co. KG (Hanau, Germany), had a chemical composition according to the ASTM F3055 standard, and it was produced by vacuum inert gas atomization (VIGA). The particle size distribution (PSD) ranged from 13 μm to 53 μm. The specimens tested in the present study were manufactured with the RenAM 500S Flex machine (Renishaw company, Wotton-under-Edge, Great Britain), which has a maximum laser power of 500 W. This machine is installed at the AM laboratory of the Department of Civil and Industrial Engineering of the University of Pisa.

The geometries of the printed specimens are reported in Fig. 1. Three types of specimens were considered in the research:

- a specimen to perform the static tensile test, Fig. 1(a);
- a cylindrical plain, designed according to the ASTM E466 standard, and a miniaturized plain specimens, both in the as-built condition and to calibrate the fatigue model, Fig. 1(b) and (c);
- a cylindrical plain specimen, designed according to the ASTM E466 standard, then machined (turning) (Fig. 1(b)) and a miniaturized notched specimen for fatigue strength predictions validations (Fig. 1(c))

The roughness symbol of Fig. 1(b), reported in brackets, indicates the obtained roughness value R_a after the machining operation by turning, while the other roughness symbol in the same sub-figure signifies that the surface of the specimen did not undergo any further machining after the printing and it is referred to the cylindrical plain specimen in the as-built condition. The turning machining operation was performed with the Haas TL1 CNC lathe. Since the material investigated in this research was a nickel-based superalloy, a correct selection of the insert to perform the machining operation by turning was necessary. A Coro-Turn TR insert, provided by Sandvik Coromant (Sandviken, Sweden), was employed, and its ISO nomenclature is: TR-VB1304-F H13 A. As reported in the Sandivk manual, regarding this specific turning tool and alloy, the cutting depth was set equal to $a_t = 0.3$ mm, the feed rate was set equal to $f_t = 0.07$ mm/round and the cutting speed was set equal to $v_t = 40$ m/min. The use of the two roughness symbols in Fig. 1(b) is motivated by the fact that the fatigue strength of cylindrical specimens in the as-built condition and after machining process by turning was investigated in this research. In Fig. 1(d) the different sizes between the cylindrical and the miniaturized specimens are highlighted. The miniaturized specimen can be tested both as a plain specimen or as a notched specimen depending on the side which undergoes tensile stress, as explained after.

The cylindrical specimens were manufactured with their axis aligned with the building direction, and, similarly, the longest side of the miniaturized specimens was along the building direction too. In this way, both types of specimens experienced the unixial strain along the additive path. The parameters employed during the 3D printing process are listed in Table 1. These parameters are the same as those employed for the baseline case in the previous paper [18], and they were found to avoid almost completely the presence of lack of fusion, internal pores and keyhole defects. The reported parameters, which are significant for the process, are: the laser power P, the scan velocity v, the hatch distance h, the layer thickness t, the meltpool aspect ratio A_r, which is defined as the ratio between the length l and the diameter $2r$ of the meltpool ($A_r = l/2r$). The values of l and $2r$ were calculated in agreement with what presented in Refs. [17,18]. Other significant parameters reported in Table 1 are the energy density (E_d), defined as $E_d = P/thv$, and the L-PBF build rate (B_r), which was computed as $B_r = thv$. For the hatching area, a stripe scanning approach was performed, and a layer rotation of 67° was imposed for each layer in order to minimize the process-induced residual stresses. On the contrary, the outer region was printed with 3 paths parallel to the outer border and performed in the same direction. The details of this printing strategy are reported in Fig. 2 for both the two specimen geometries (Fig. 1(b) and (c)). All specimens were printed in a single batch, with

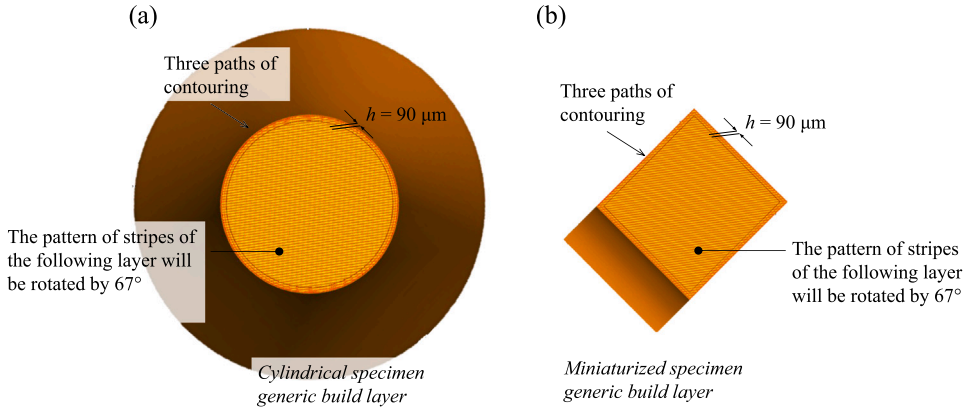

Fig. 2. Stripe and contour imposed paths for the cylindrical (a) and miniaturized (b) specimens.

Table 1
Parameters used in the L-PBF process.

P (W)	v (m/s)	h µm	t µm	A_r –	E_d (J/mm^3)	B_r (mm^3/s)
280	0.9	90	60	5	57.6	4.9

Table 2
Static mechanical properties of the aged Inconel 718.

	μ_t	σ_t/μ_t
S_Y (MPa)	1085	1%
S_U (MPa)	1340	1%
ϵ_f (%)	16	10%
E (GPa)	155	3%

the build plate heated at 170 degrees Celsius to minimize residual stresses. The process chamber was filled with Argon gas, ensuring an Oxygen concentration of less than 7 parts per million by weight, thus preventing oxidation. Upon removal from the printing plate, no visible distortion was observed in any of the specimens.

Right after, the specimens underwent an aging heat treatment process, which, as clearly shown in Ref. [18], provided a considerable increase of hardness with respect to the not aged specimens. The aging treatment involved a Nabertherm LH/120 furnace equipped with a protective gas enclosure that again was consistently purged with Argon gas to prevent oxidation. Additionally, the furnace was equipped with a controlled cooling system to impose any heat treatment. The heat treatment, consistent with AMS 5663 standard and Ref. [20], was applied to all the specimens and it was composed of two phases: the solutioning phase and the double aging phase. In the first phase the specimens were maintained at a temperature of 980 °C for 1 h, then they underwent a forced furnace cooling until 50 °C, whereas in the second phase a new heating up to 720 °C for 8 h was applied, followed by a furnace cooling with a decreasing rate of 55 °C/h until 620 °C and a final 8 h/air cooling. In this research, all the specimens were heat treated in an unique batch right after the printing phase. In Refs. [65,66], the surface residual stresses were measured for specimens made of Inconel 718, obtained by L-PBF, even with similar printing parameters and same aging treatment employed in this research, and almost null values were obtained. According to this latter consideration, in this research the influence of the residual stresses on the fatigue behaviour was considered negligible. The machined specimens were turned after the heat treatment. In Fig. 3 the obtained specimens through the L-PBF technique are reported: Fig. 3(a) presents the specimens obtained immediately after the printing, while Fig. 3(b) shows the specimens within the furnace for the aging treatment. As shown in Fig. 3, the placement of the samples was consistent with the goal of minimizing sample distortions during heat treatment, and, as a consequence of the applied heat treatment, no process-induced residual stresses are present in the tested specimens.

2.2. Mechanical tests

Different tests were performed to characterize the mechanical behaviour of the material, in particular tensile testing, fatigue testing and hardness testing were carried out. The tensile test was conducted at room temperature and by means of an MTS servohydraulic machine with a maximum load capacity of 50 kN, equipped with an extensometer having a gauge length of 10 mm. The test was performed on the specimen shown in Fig. 1(a) with an initial strain rate of 1×10^{-4} s^{-1}. The mean values μ_t of the static mechanical properties, extracted from the tensile testing, together with the corresponding ratio between the standard deviation σ_t and the mean value are reported in Table 2.

Fatigue tests of cylindrical specimens presented in Fig. 1(b) (both as-built and machined) were conducted at room temperature using an axial loading configuration on a RUMUL Mikrotron resonant testing machine, and the imposed load ratio was $R = 0$. The test frequency was monitored to identify the onset of macroscopic crack propagation, by observing the resulting decrease in specimen stiffness, and it was of the order of 100 Hz. The tested cylindrical specimen featured a uniform diameter along the gauge length, as shown in Fig. 1(b). This design allowed for a large area exposed to consistent high stress.

The fatigue tests on the miniaturized specimens were performed on the Mini FP2 machine [57], which is presented in Fig. 4(a) while performing fatigue tests at the Department of Engineering and Architecture of the University of Parma. More details about the various components of the MiniFP2 machine can be found in Ref. [67]. Given that this kind of specimen has a plain and a notched sides (Fig. 1(c)), in this research both sides were tested and investigated. As qualitatively explained in Fig. 4(b) and (c), the employed machine has an oscillating grip at one end which allows to rotate one extremity of the specimens providing a bending moment, whereas the opposite grip maintained the specimens fixed to the frame. The fatigue tests were performed at room temperature with a load ratio $R = 0$ and at a frequency of the order of 25 Hz.

$$\sigma_a = k N_f^b \tag{1}$$

$$\sigma_f = \sqrt{\frac{\sum_{i=1}^{N} \left(\sigma_{a,i} - \hat{\sigma}_{a,i}\right)^2}{N - q}} \tag{2}$$

The relationship between the cyclic bending moment and the amplitude stress σ_a generating the fatigue stress loading, in the miniaturized specimens, was accurately considered in this study. The nominal maximum stress can be found by means of the beam equation: $\sigma_{nom.,max} = 6M/W$, where M is the applied bending moment monitored by the test

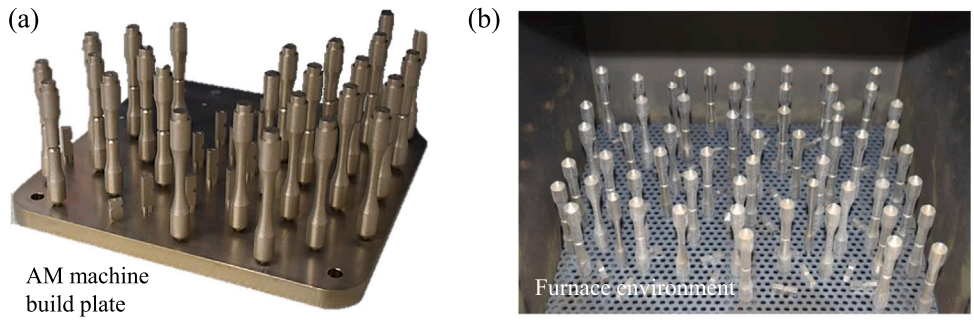

Fig. 3. Specimens produced by the L-PBF technique: (a) after the 3D printing, (b) inside the furnace ready for the aging treatment.

machine load cell, and W is the bending section modulus computed as $W = BH^2/6$, where B and H are the width and height of the miniaturized specimen minimum cross-section (nominally, $B = H = 5$ mm). In the unsymmetrical minimum cross-section of the miniaturized specimen, the stress distribution deviates from the Navier linear distribution. Finite element (FE) analyses, performed on AnsysWorkbench software, were used to determine the elastic stress distribution under bending. After comparing the maximum stress $\sigma_{real,max}$ of the plain side to the corresponding nominal stress value $\sigma_{nom.,max}$, it was evident that $\sigma_{real,max}$ is 9% lower than $\sigma_{nom.,max}$. To account for this deviation, a correction factor for the miniaturized plain specimen geometry C_{mg} was introduced, which was obtained as $C_{mg} = \sigma_{real,max}/\sigma_{nom.,max} = 0.91$, and this factor was applied to $\sigma_{nom.,max}$, calculated analytically as M/W. The obtained value of $\sigma_{real,max}$ was then used to calculate the amplitude stress representative of the fatigue strength of the miniaturized plain specimen. A similar approach was applied to the notched side of the miniaturized specimen. The bending moment leading to failure was monitored by the machine load cell, and the obtained value was then introduced as input for the FE analyses, to investigate the corresponding amplitude stress at the notch root. The maximum value of this stress, obtained by FE analyses in the notch region, was considered as the fatigue strength of the miniaturized notched side.

The S-N curves of the cylindrical and the miniaturized specimens are reported in Fig. 5 where the solid lines indicate the curves at 50% probability of failure, while the dashed lines represent the curves at either 90% or 10% of probability of failure. The curves at 50% probability of failure were calculated with a least squares fit of the Basquin law (Eq. (1)) on the experimental data, where σ_a indicates the stress amplitude, k and b are the Basquin parameters and N_f indicates the number of cycles to failure. The values of the standard deviations σ_f for the fatigue tests were calculated according to Eq. (2). In this latter equation $\sigma_{a,i}$ is the i–th stress amplitude data point, $\hat{\sigma}_{a,i}$ is the estimator, N is the number of data points included in the fit and q is the number of parameters to characterize the used fitting curve, which is 2 for the Basquin law. Given that the number of cycles of the miniaturized specimens fatigue data of did not overcome 2×10^6 cycles, as shown in Fig. 5, a unique fatigue limit was just fixed at 2×10^6 cycles. The values of the fatigue strength amplitude at this number of cycles (50% of probability of failure) for the as-built cylindrical, the machined cylindrical, the miniaturized plain and the miniaturized notched specimens are reported in Table 3. The estimated numerical values of the parameters of the Basquin law, the standard deviation and T_σ for each kind of specimens are also reported in Table 3. The T_σ was defined as the ratio between the values of the fatigue limit, obtained from this fitting procedure, at 90% of probability of failure and at 10% of probability of failure.

Vickers hardness tests were also conducted for the additively manufactured specimens. The hardness test was performed with an AFFRI hardness tester, applying a load of 10 kg for a duration of 10 s. To ensure accuracy, the measurements were taken at a distance of at least 2.5 and 3 times the diagonal length of the indentation from both the specimen contour and any adjacent measurement. These testing practices complied with the ISO 6507 standard, and a value of approximately $H_V = 457$ HV was obtained at the end of the measures. This latter value is coherent with that obtained in the previous research [18].

2.3. Microstructural analysis

Metallographic analyses were conducted to examine the microstructure obtained after the AM and the aging processes. The specimens were prepared according to the ASTM E3-11 standard and were subjected to etching using Kalling's II (n.94, ASTM E407). In order to investigate the specimen porosity, optical microscope (OM) observations were taken along the specimen longitudinal direction, which are shown in Fig. 6. In Fig. 6(a) and (b) a typical view of the microstructures of cylindrical and miniaturized specimens, respectively, are reported in correspondence of the external surface. Few pores were observed at a distance from the external surface, and their circular shape suggests that they were originated from entrapped gas bubbles.

In Fig. 6(a) and (b), it is possible to observe the typical grains shape of specimens produced by L-PBF. Within the outer 10 μm, the thermal gradient perpendicular to the surface generated a fine-grained dendritic microstructure. The grains are elongated along the building direction and the mean aspect ratio, defined as the ratio between the longitudinal and transverse grain dimensions, was found to be $A_{r,g} = 0.25$. The same grain orientation and dimensions were found in the cylindrical and in the miniaturized specimens. The bulk material solidification was governed by the thermal gradient directed as the L-PBF build direction, for both specimens. In Fig. 6(c) it is possible to observe the microstructure of the bulk zone of the miniaturized specimen. The grains are still stretched along the building direction and the aspect ratio is still almost $A_{r,g} = 0.25$. These characteristics confirm the homogeneity of the specimens between the zone in correspondence of the external surface and the bulk zone. The calculated mean values of the aspect ratio and the orientation of the grains were coherent with the corresponding results obtained in Refs. [68,69]. In these latter papers, in fact, the samples were produced by L-PBF with similar parameters as those of this research, and after they underwent an equivalent aging treatment.

2.4. Fractographic analyses

Fractographic analyses were carried out by scanning electron microscopy (SEM) on specimens after fatigue failure, and some of the obtained results are reported in Fig. 7. They show that the crack initiation occurred typically in correspondence of a surface roughness valley as shown in Fig. 7(a) for an as-built cylindrical specimen; sometimes the crack initiation was still found in correspondence of a roughness valley, but this was probably due to combinations between defects and surface roughness as shown in Fig. 7(b) and (c), for a machined cylindrical and a miniaturized plain specimens, respectively.

In Fig. 7(c) it is highlighted the typical crack initiation of the miniaturized plain specimen, which was found at a roughness valley in

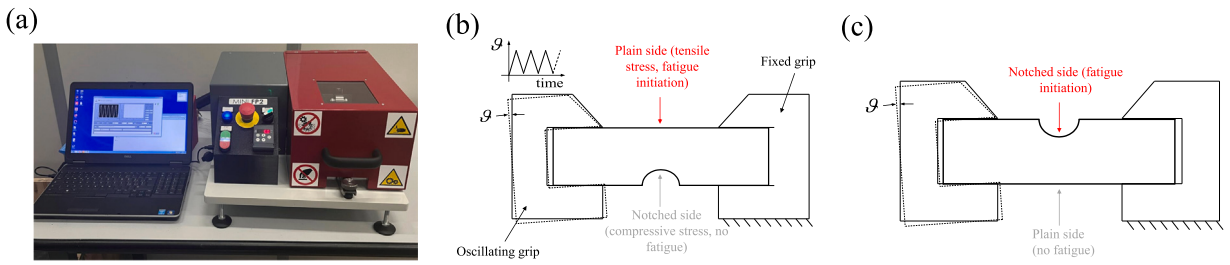

Fig. 4. (a) Image of the Mini FP2 machine while performing fatigue tests and schematic illustrations about the working principle of the Mini FP2 machine: (b) test of the plain side and (c) test of the notched side.

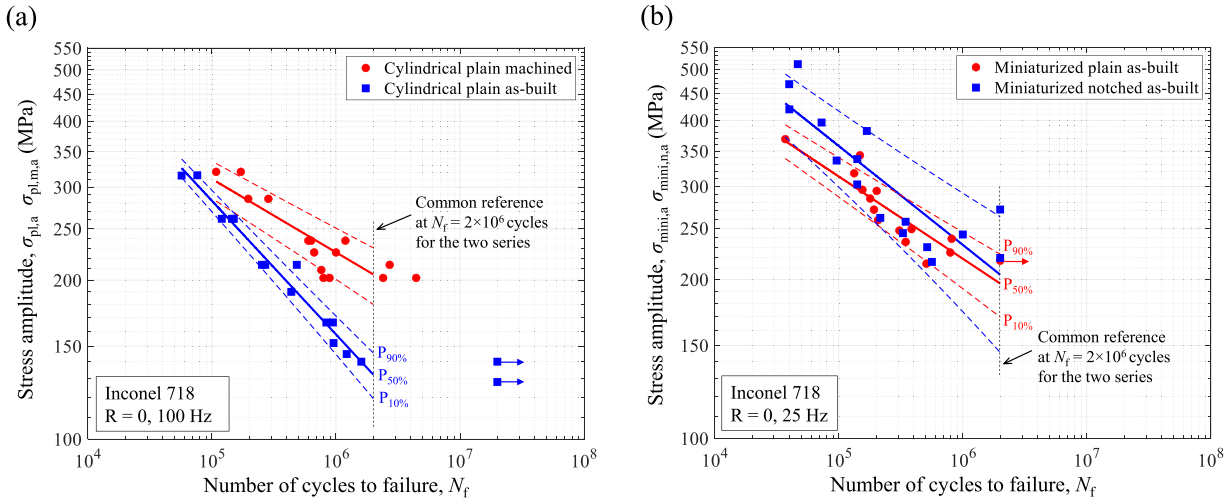

Fig. 5. (a) S-N curves of the cylindrical plain (as-built and machined) and (b) the miniaturized plain and notched (as-built) specimens.

Table 3
Principal numerical values obtained from the fitting operation on the experimental fatigue data.

Specimen type	Fitted Basquin law	Exp. Fatigue limit, 2×10^6 cycles (MPa)	σ_f (MPa)	T_σ
Cylindrical as-built	k = 5200 MPa, b = −0.253	132	10.3	1.22
Cylindrical machined	k = 1540 MPa, b = −0.139	205	19.6	1.28
Miniaturized plain as-built	k = 1880 MPa, b = −0.156	196	20.9	1.32
Miniaturized notched as-built	k = 3090 MPa, b = −0.187	204	45.8	1.81

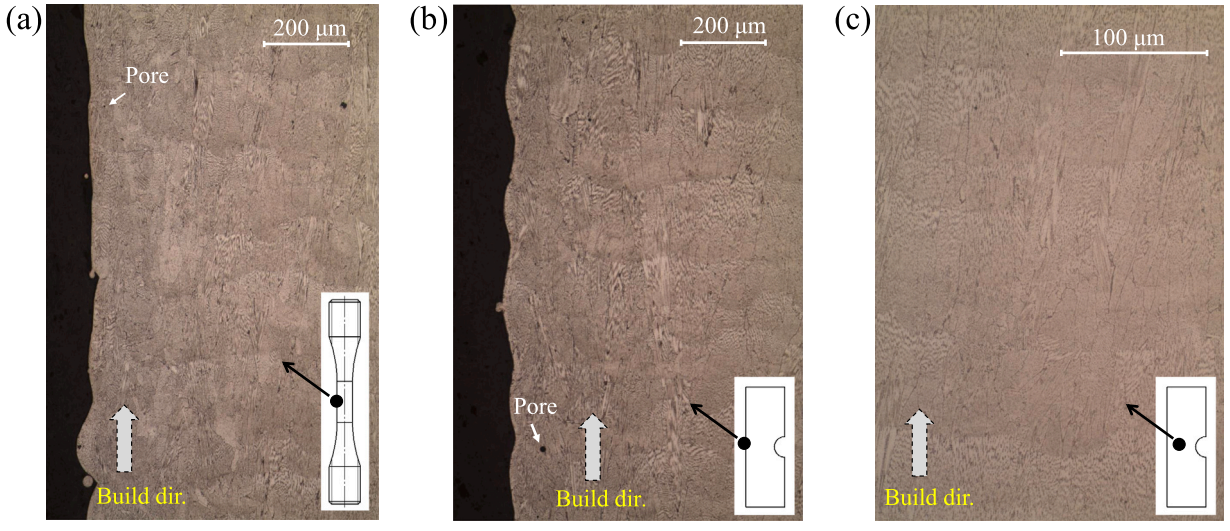

Fig. 6. Microstructure analyses after the aging treatment of the specimens: (a) external surface observation of an as-built cylindrical specimen, (b) external surface observation of a miniaturized specimen, (c) bulk observation of an as-built miniaturized specimen.

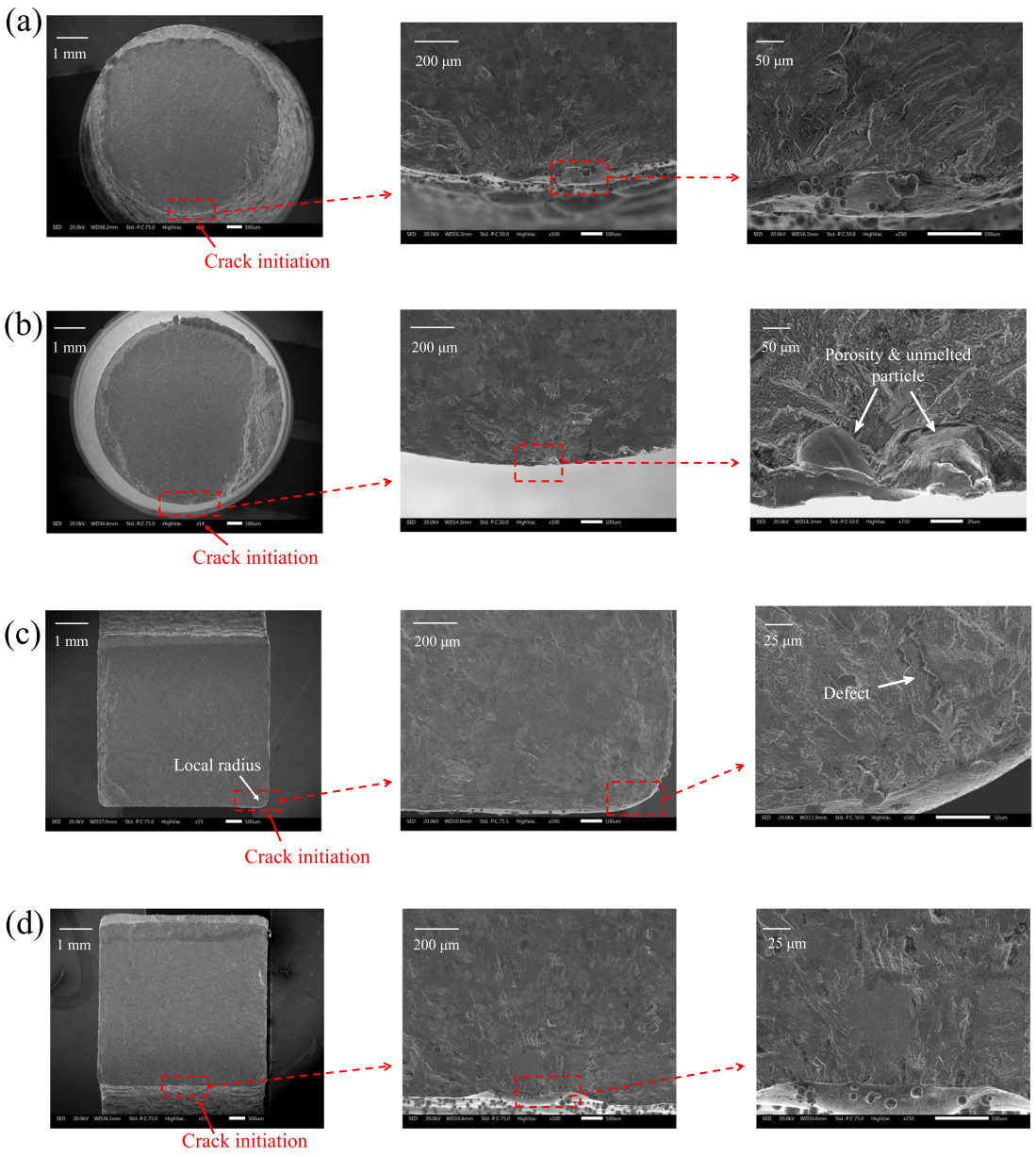

Fig. 7. SEM fractography images of as-built cylindrical specimen (a), machined cylindrical specimen (b), miniaturized plain specimen (c) and miniaturized notched specimen (d).

correspondence of the edge between the surface referred to the plain side and the two lateral surfaces. In the same sub-figure it is also shown the presence of a fillet radius in correspondence of the crack initiation zone. In Fig. 7(d) the fractographic analysis of a miniaturized notched specimen is presented, and the crack initiation was typically prone to initiate at a roughness valley near the centre of the section. In all the cases the crack propagation was found to be approximately perpendicular to the loading direction as typical for Mode I fracture behaviour.

2.5. Determination of the highly stressed surface

The highly stressed surface (HSS) was determined by FE simulations of the cylindrical and the miniaturized specimens. The HSS was defined as the area approximately exposed to an axial stress equal or higher than the 90% of a reference axial peak stress. In the cylindrical specimen the stress was determined by the application of an axial load, and the corresponding HSS is indicated in red in Fig. 8.

In the miniaturized specimens a bending moment was applied, and this was coherent with the loading experienced during the fatigue tests. For the miniaturized plain specimen the results of the FE simulations to obtain the value of the HSS are presented in Fig. 9. Firstly, a global model, realized exploiting the two geometric symmetries of the specimen, was realized, then the local stress in the area of interest was better analysed with the submodelling technique. For this kind of specimen, considering what found out with the fractographic images (Fig. 7(c)), the reference value of the peak stress was taken at the intersection between the fillet radius, which was included in the FE simulations to provide better accuracy, and the surface referred to the plain part of the specimen (Point A, Fig. 9). To calculate the value of the HSS, we considered that, as reported in Fig. 9 by a 2D map of the scanned surface, a high value of the surface roughness was found within an extension of approximately 0.5 mm starting from the intersection between the surface referred to the plain part and the fillet radius. Finally, the value of the HSS was calculated by combining the area where the stress was included in the range given by the reference peak stress and the corresponding value at 90% with the area of a rectangle, taken on the surface referred to the plain part, whose one dimension was equal to 0.5 mm and the other dimension was found to

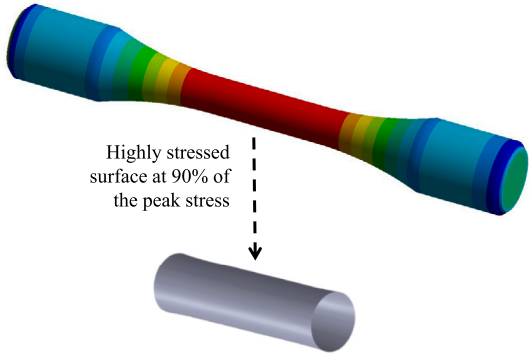

Fig. 8. Highly stressed surface of the cylindrical plain specimen.

include in the rectangle the points experiencing an axial stress equal or higher than the 90% of the reference peak stress. The results of the FE simulations to obtain the HSS of the miniaturized notched specimens are presented in Fig. 10. As done for the miniaturized plain specimen a first global model exploiting the geometric symmetries of the specimen was realized, then the local stress near the centre of the notched zone was investigated by the submodelling technique and finally the numerical value of the HSS was calculated. In this case, the reference value of the peak stress was taken as the maximum value of the axial stress obtained with the simulations.

The percentage of the reference peak stress (90%) for the HSS was established to include the usual crack initiation point of the miniaturized notched specimen, which was found not exactly at the central point of the notch along the axial direction. If the percentage of the reference peak stress had been fixed at 95% or at 99%, the crack initiation point of the miniaturized notched specimen would not have been included in the HSS, thus resulting in a not physical implementation of the criterion. The obtained values of the HSS for the cylindrical plain, for the miniaturized plain and for the miniaturized notched specimens were: S_{pl} = 469 mm^2, S_{mini} = 5.50 mm^2 and $S_{mini,n}$ = 3.30 mm^2, respectively.

2.6. Optical profilometer observations

The surface roughness was analysed through the optical profilometer (OP) Taylor Hobson CCI MP-L, which is based on the coherence correlation interferometry. This latter consists of a light source divided into two paths, and among them one moves to a reference surface and the other moves to the test surface. The two reflected rays of light combine in correspondence of a camera detector where their interference fringes reproduce the surface topography. For all the kinds of specimens, i.e. cylindrical as-built, cylindrical machined, miniaturized plain and miniaturized notched, several specimens were scanned in correspondence of the HSS presented in paragraph 2.5.

The surface roughness was investigated in the central part of the cylindrical specimen, which corresponded to the HSS, Fig. 11. The observations of the cylindrical as-built specimens were carried out varying the θ angle, indicated in Fig. 11, from 0° to 360° with steps of 45°.

On the other hand, the miniaturized plain specimens were analysed within the HSS and in particular in correspondence of the edge between the surface referred to the plain side and the lateral surfaces given that the crack initiation was observed in this zone, as shown in Fig. 7(c). An image of the profilometer while performing the surface profiles acquisitions, of the miniaturized plain specimen, is reported in Fig. 12(a) and a typical observation of the miniaturized plain specimen is reported in Fig. 12(b).

The machined cylindrical specimens were also investigated within the corresponding HSS, which is the same as that of the cylindrical as-built specimens. For this latter specimen the scans were not conducted varying the θ angle, as for the as-built ones, because a uniform surface roughness varying with the θ angle was expected due to the machining operation by turning. The typical scan of the machined cylindrical specimen is reported in Fig. 13.

Finally, the surface roughness of the miniaturized notched specimens was analysed as shown in Fig. 14. The metallographic analysis of Fig. 14(a) shows that typically a more severe roughness condition was found in the upskin zone of the miniaturized notched specimen and not in correspondence of the exact centre. This latter justifies why the crack did not initiate exactly at the centre of the notch, and it also justifies why the observations carried out with the OP (Fig. 14(b)) were mostly focused on this zone for this kind of specimen. In Fig. 14(c) a typical surface acquisition of a failed miniaturized plain specimen is also reported, and an evident crack initiation at a roughness valley is shown.

The surface profiles obtained from the 3D optical profilometer were not filtered to separate the waviness from the surface roughness. As shown in Figs. 11, 12, 13 and 14, the sampling length was lower than 2.5 mm, thus the waviness was not even included in the acquisitions according to ISO 4288. The only employed data manipulation was a second-order polynomial form that was necessary to remove the effects of the curvature in the cylindrical specimens. Several areal parameters, such as S_q, S_{sk}, S_{ku}, S_p, S_v, S_z and S_a, were calculated from the 3D scans according to ISO 25178. S_q indicates the root mean square of the heights of the selected area, S_{sk} is the skewness parameter to describe the symmetry of the scanned portion with respect to the mean surface, S_{ku} is the Kurtosis parameter to describe the sharpness of the roughness profile, S_p indicates the maximum peak height, S_v indicates the maximum valley depth, S_z indicates the sum of the maximum peak height and the maximum valley depth and finally S_a indicates the arithmetic mean of heights of selected area. These parameters of some of the investigated specimens are reported in Table 4. It is important to highlight that the attached powder particles might influence the roughness parameter. However, as highlighted in Ref. [46], the attached powder particles have no considerable impact on the stress.

Table 4
Numerical values of S_q, S_{sk}, S_{ku}, S_p, S_v, S_z and S_a for some of the four kinds of specimen and calculated according to ISO 25178.

Specimen type	S_q (μm)	S_{sk}	S_{ku}	S_p (μm)	S_v (μm)	S_z (μm)	S_a (μm)
Cylindrical as-built 1	12.3	0.0576	2.12	43.2	29.3	72.5	10.4
Cylindrical as-built 2	11	0.136	2.39	38.4	32.9	71.3	9.34
Cylindrical as-built 3	6.91	0.954	5.82	56.4	19.3	75.7	5.27
Cylindrical as-built 4	7.88	0.292	4.68	41.2	36.8	78.0	6.10
Miniaturized plain as-built 1	9.19	0.426	3.37	52.7	28.0	80.7	7.33
Miniaturized plain as-built 2	10.9	1.27	6.73	63.8	31.3	95.1	8.06
Miniaturized plain as-built 3	8.51	−0.178	5.22	37.5	48.6	86.1	6.32
Miniaturized plain as-built 4	7.18	0.509	4.11	50.5	30.2	80.7	5.60
Cylindrical machined	0.569	−0.126	2.71	5.78	2.43	8.21	0.463
Miniaturized notched as-built	8.69	0.943	4.70	47.9	29.4	77.3	6.30

3. Fatigue strength prediction

3.1. Murakami model for the surface roughness

The fractographic analyses presented in Fig. 7 show that the crack initiation occurred in correspondence of a surface roughness valley, and combinations between defects and surface roughness can also be responsible for fatigue failure, as shown in Fig. 7(b) and (c) for a machined cylindrical and a miniaturized plain specimens, respectively. Fig. 14(c) also shows that the crack initiation was more prone to start in correspondence of a roughness valley.

The original expression developed by Murakami [52], proposed for symmetric reversal loading ($R = -1$), is reported in Eq. (3) to model the role of the defects on the fatigue limit. In this equation the factor 1.43 is

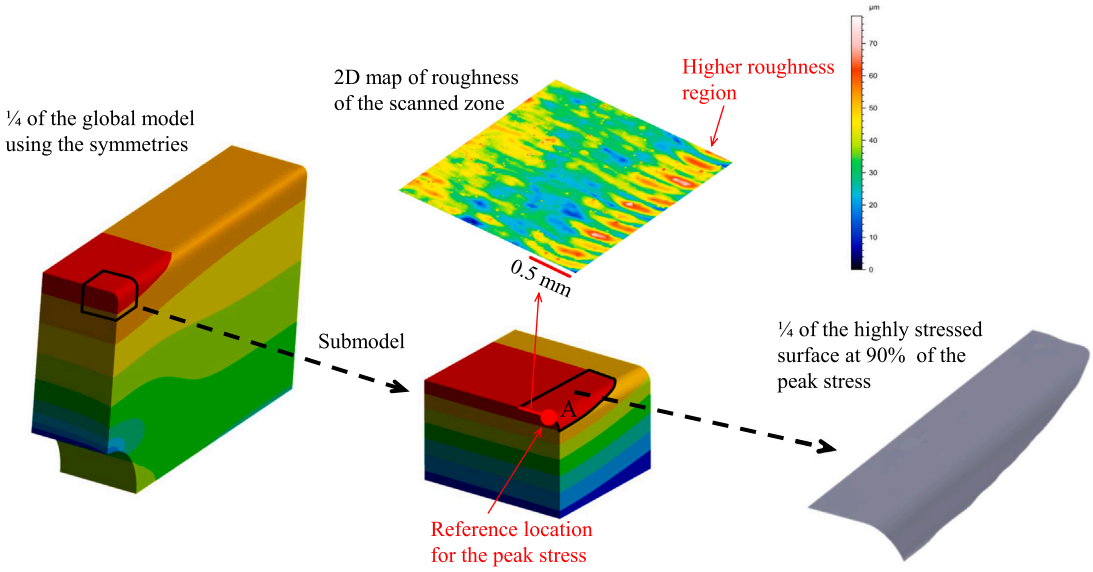

Fig. 9. Highly stressed surface of the miniaturized plain specimen.

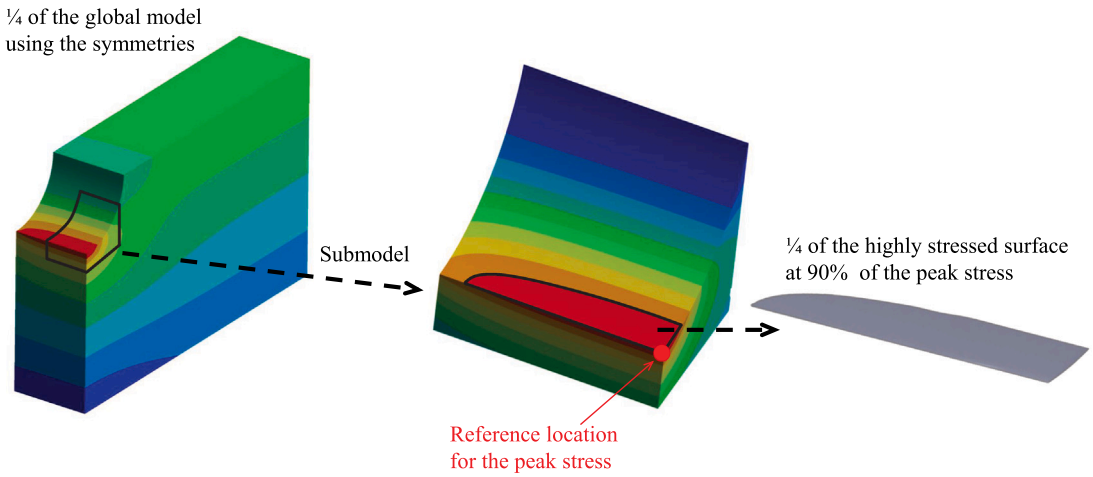

Fig. 10. Highly stressed surface of the miniaturized notched specimen.

used when the fatigue strength is mostly influenced by surface defects, and H_V indicates the Vickers hardness. As explained in Ref. [64], there could be two other different equation factors rather than 1.43: the factor 1.41 is generally used for defects tangent to the surface, while the factor 1.56 is used for the presence of internal defects. However, the loadings were asymmetric in this research, thus it was necessary to add a corrective factor to the Murakami expression just to account for the mean stress effect. Considering that only tensile loadings were investigated, a corrective factor inspired by the SWT fatigue criterion [18,37,70] was employed, and it is introduced together with the modified Murakami expression in Eq. (4).

In Ref. [52], Murakami also investigated the effects of surface roughness on the fatigue limit, stating that it is governed by the threshold of a non propagating crack located at a valley for specimens in which the surface roughness is more critical than the internal defects. Considering the linear elastic fracture mechanics (LEFM) for a crack in an infinite solid, which is under remote tensile stress perpendicularly oriented with respect to the crack length, the mode I stress intensity factor can be obtained with Eq. (5). In this latter equation, F is the geometric correction factor. In order to consider the effect of inclusions on fatigue strength, in Ref [64]. Murakami proposed a relationship between the mode I stress intensity factor and the area of the defects, which is presented in Eq. (6), where the multiplicative coefficients 0.65 is valid for the surface defects. By combining Eqs. (5) and (6), Eq. (7) was obtained, which is a relationship between the term $\sqrt{area}$ and the geometric correction factor F. In Ref [71]. Murakami investigated the trend of the geometric correction factor F for periodic surface cracks in a semi-infinite body depending on the depth a (with respect to the external surface) and on the pitch p of the cracks. The obtained relationship between the geometric factor F and a and p was substituted in Eq. (7), thus obtaining Eq. (8). By modelling the surface profile as a periodic sequence of cracks, Eq. (8) can then be applied to obtain an equivalence between the term $\sqrt{area_R}$ and the surface roughness. In Eq. (8) it is highlighted the effect on the fatigue strength of both the pitch distance p, between two consecutive roughness valleys, and the depth a. However, the influence of the valley depth is no longer effective when the ratio between the depth a and the pitch p becomes higher than a certain value.

$$\sigma_w = \frac{1.43\left(H_V + 120\right)}{\left(\sqrt{area}\right)^{1/6}} \tag{3}$$

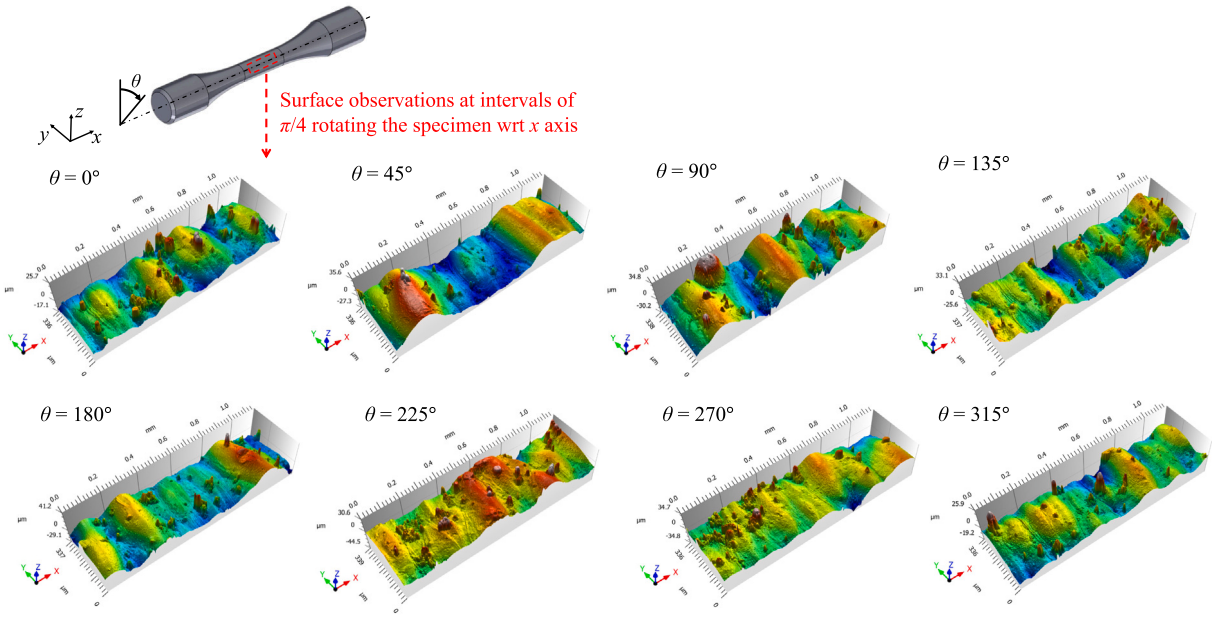

Fig. 11. Surface acquisitions of an as-built cylindrical specimen.

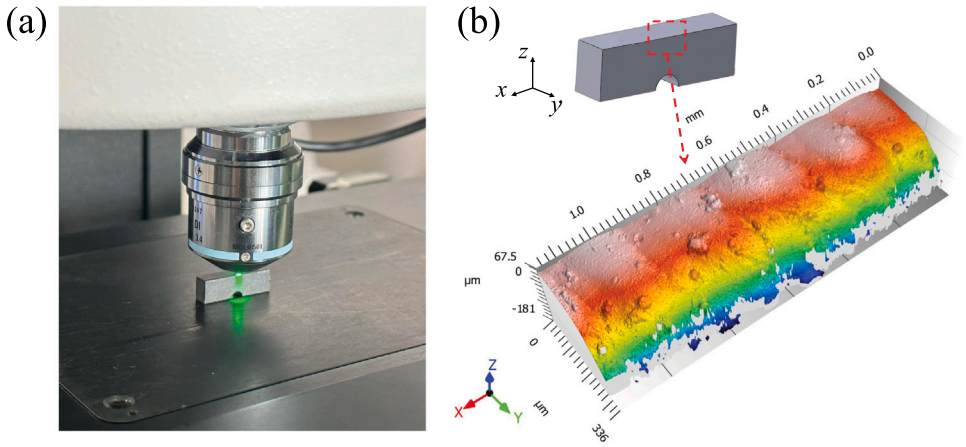

Fig. 12. (a) Profilometer while performing surface scans and (b) surface profiles analyses of a miniaturized plain specimen.

$$\sigma_{w,\ R\neq -1} = \sigma_{w,\ R=-1}\left(\frac{1-R}{2}\right)^{1/2} \tag{4}$$

$$\sigma_{w,\ R\neq -1} = \frac{1.43(H_V+120)}{\left(\sqrt{area}\right)^{1/6}}\left(\frac{1-R}{2}\right)^{1/2}$$

$$\Delta K_I = F\Delta\sigma\sqrt{\pi a} \tag{5}$$

$$\Delta K_I = 0.65\Delta\sigma\sqrt{\pi\sqrt{area}} \tag{6}$$

$$\sqrt{area} = a\left(\frac{F}{0.65}\right)^2 \tag{7}$$

$$\sqrt{area_R} = \begin{cases} p\left(2.97\left(\frac{a}{p}\right) - 3.51\left(\frac{a}{p}\right)^2 - 9.74\left(\frac{a}{p}\right)^3\right) & \text{if} \quad \frac{a}{p} < 0.195 \\ 0.38p \quad \text{if} \quad 0.195 < \frac{a}{p} < 3 \end{cases} \tag{8}$$

3.2. Analytical reproduction of the surface profile

When an irregular surface profile is analysed, the definition of the two quantities a and p to use in Eq. (8) is not straightforward. For example, in Ref. [46] a roughness profiler was employed to obtain the main roughness parameters, then the value of a was set equal to R_v, which is the maximum valley depth according to ISO 4288. In this study, given the intrinsic irregularity of the surface morphology, the profiles of the investigated specimens were approximated by the sum harmonics, which were extracted by means of the fast Fourier transform (FFT). After this, the values of p were calculated as the distance of two consecutive valleys, while a was obtained as the highest difference of height between a peak and the two adjacent valleys.

Different scans were taken on the as-built cylindrical specimens in the HSS, by varying the angle θ as presented in Fig. 11. For each orientation some profiles were selected trying to avoid including the attached powder particles, which could result as undesired peaks of the surface profiles, and then the corresponding values of a and p were calculated to be used in the Murakami formula. The surfaces of the miniaturized plain specimens were scanned next to the edges between the upper surface, referred to the plain part of the specimen, and the

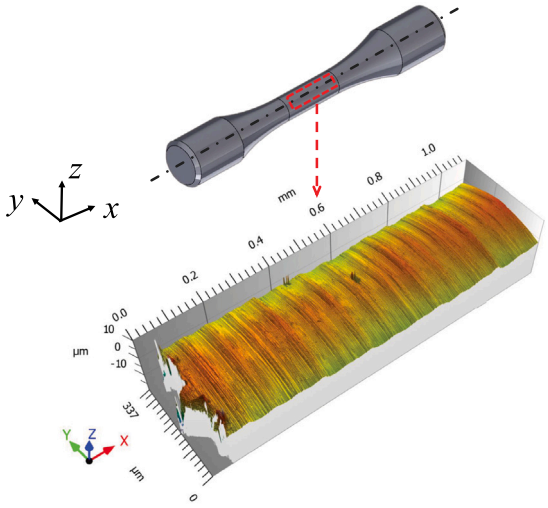

Fig. 13. Surface acquisition of a machined cylindrical specimen.

two lateral surfaces as shown in Fig. 12(a). The profiles considered relevant for the fatigue analyses were that in correspondence of the edge because, as shown in the fractographic analyses of Fig. 7(c), the crack initiation was typically located there. Some profiles to be modelled with the FFT were also extracted from the highly stressed surfaces of the cylindrical machined and of the miniaturized notched specimens. In Figs. 15, 16, 17 and 18 some examples of the raw data with the modelled profiles, obtained through the FFT, are presented for the cylindrical as-built, the miniaturized plain, the cylindrical machined and the miniaturized notched specimens, respectively. It is important to highlight that, from the scanned surfaces, the analysed profiles were extracted in the plane $x - z$ given that the external load was aligned with x direction. This latter was coherent with what stated by Murakami [64]. For the miniaturized notched specimen, as shown in Figs. 14 and 18(a), the scanned surface was typically not horizontal given that the investigated surface was near the upskin region characterized by a worse surface roughness. Because of this and for the sake of simplicity, the selected profiles were rotated with respect to the y axis, as indicated in Fig. 18(b), in order to reach a horizontal configuration. In Fig. 16(b) a graphical explanation of the meaning of a and p is provided.

The number of harmonics to correctly reproduce the experimental profiles was chosen as a trade-off between the aim to exhaustively reproduce the raw data and to avoid the presence of a high number of harmonics, which could generate undesired and not physically meaningful oscillations. For the as-built specimens, the values of the maximum frequencies, included in the set of harmonics considered for the modelling of the surface profiles, were very similar. For the machined specimens, the value of the maximum frequency, of the set of harmonics considered for the modelling of the profile, was higher than the corresponding of the as-built specimens as shown in Fig. 17(b). This latter because lower values of the pitch were generated by the turning machining. Once the modelled profiles were obtained, their peaks and valleys positions were found, and they are marked by red and black points in Figs. 15(b), 16(b), 17(b) and 18(b), respectively.

3.3. Proposed model for fatigue strength predictions

Once the profiles were approximated by the sum of harmonics, the values of a and p were obtained for each analysed scan of the cylindrical and the miniaturized specimens. It is important to remark that a was calculated as the highest difference of the z coordinates between a red point and the two adjacent black points in Figs. 15(b), 16(b), 17(b) and 18(b). The corresponding value of p was determined as the difference of the x coordinates of the two black points employed during the determination of a. This approach was required to be clearly defined, provided that the obtained (as-built) surface roughness resulted irregular to some extent, rather than the machining surface roughness (such as obtained as turning) which is more periodic. The obtained couples of a and p were then employed in the Eq. (8) to calculate the values of $\sqrt{area}_{\mathrm{R}}$. Among all the performed surface roughness measurements, the values of a and p which resulted in the highest value of $\sqrt{area}_{\mathrm{R}}$ were identified for the cylindrical and the miniaturized specimens.

The obtained quantities were: $\sqrt{area}_{\mathrm{R,\,1}} = 116$ μm, $\sqrt{area}_{\mathrm{R,\,2}} = 105$ μm, $\sqrt{area}_{\mathrm{R,\,3}} = 6.75$ μm, and $\sqrt{area}_{\mathrm{R,4}} = 66$ μm for the as-built cylindrical, the miniaturized plain, the machined cylindrical and the miniaturized notched specimens, respectively. It is important to highlight that the as-built cylindrical and the miniaturized plain specimens reported almost the same values of $\sqrt{area}_{\mathrm{R}}$. Given the inherent irregularity of the as-built roughness, and considering that the investigated surface through the OP represented a small portion of the highly stressed surface, the killer defect could be located away from this zone. In addition to this, the surface roughness could not be the only responsible for the fatigue initiation, while on the contrary a combined effect of surface roughness and sporadic defects located near the surface can be the most critical condition in terms of fatigue resistance. A significant point to investigate was that the cylindrical specimen, with an usual size for a laboratory specimen, and the miniaturized specimen would present the same fatigue strength, just according the Murakami model, since they feature very similar value of $\sqrt{area}_{\mathrm{R}}$, and obviously same roughness too. However, the different sizes between the two specimens influenced their fatigue strength properties. In Fig. 5 it is highlighted that the values of the fatigue limits of the cylindrical as-built and the miniaturized specimens are noticeably different. The higher fatigue strength of the smaller specimen is well in agreement with the size effect, since the probability to find a killer defect becomes lower. Thus, the approach proposed by the authors in this study, is to reformulate the Murakami model as reported in Eq. (9), including the size of the HSS.

$$\sigma_{\mathrm{w}} = \frac{1.43\left(H_{\mathrm{V}} + 120\right)}{\left(\sqrt{area}_{\mathrm{R}}\right)^{1/6}} \left(\frac{1-R}{2}\right)^{1/2} \left(\frac{S_0}{S}\right)^{m} \tag{9}$$

In Eq. (9) σ_{w} is the predicted value of the fatigue limit, which is the result of the combination of various terms:

- 1.43 is the usual multiplicative coefficient for surface defects,
- $\left(H_{\mathrm{V}} + 120\right)$ is the usual hardness term,
- $\sqrt{area}_{\mathrm{R}}$ includes the effects of surface roughness according to Eq. (8),
- $\left((1-R)/2\right)^{1/2}$ introduces the effect of a nonzero value of the average stress,
- $\left(S_0/S\right)^{m}$ accounts for the size effects.

In this latter equation, S corresponds to the HSS, and the term $\left(S_0/S\right)^{m}$ recalls the well-known highly stressed volume (HSV) model proposed by Kuguel in Ref. [72], in which the volumes were replaced with surfaces as discussed below. After its initial proposal by Kuguel, the HSV model was validated for smooth specimens by Khöler in Ref. [73] and it was extended to notched specimens by Böhm in Ref. [74]. Nowadays, this modelling approach is an efficient and recognized tool for fatigue strength predictions accounting for the size effect as clearly highlighted in several recent papers, such as Refs. [75–81]. Replacing the volume with the surface in Eq. (9) was motivated by the fact that the fatigue initiation was mostly observed at the surfaces, as confirmed by the fractographic analyses presented in Fig. 7. The term $\left(S_0/S\right)^{m}$ was introduced to consider the different values of the HSS between the miniaturized specimens and the typical size of the cylindrical specimens, which implies a different probability of finding a killer defect. The added term also aims to consider the fact that the scanned region corresponds to a small portion of the HSS. According

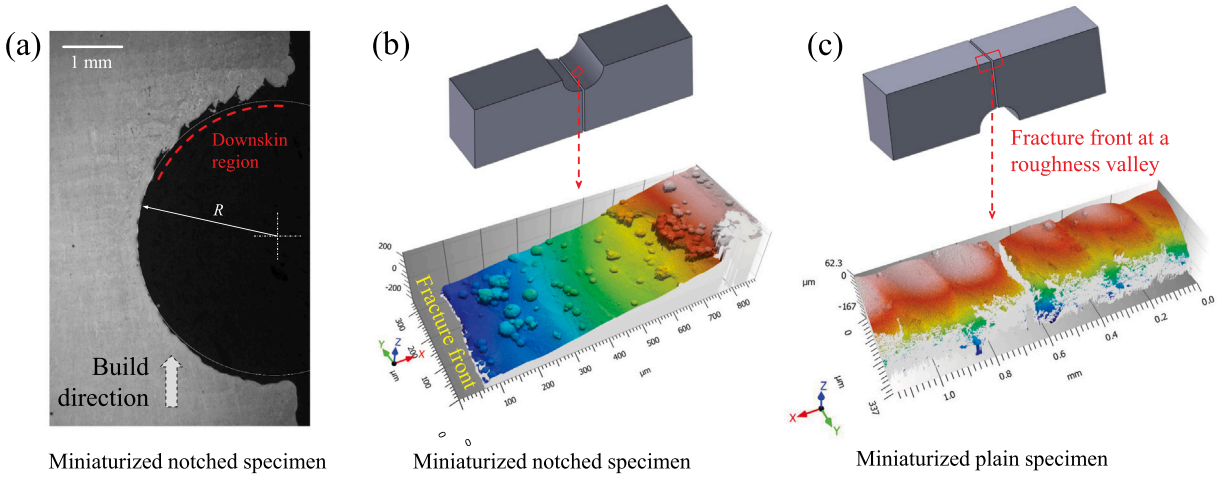

Fig. 14. (a) Typical metallographic analysis of miniaturized notched specimens, (b) scan of a miniaturized notched specimen near the crack initiation point, (c) scan of a failed miniaturized plain specimen.

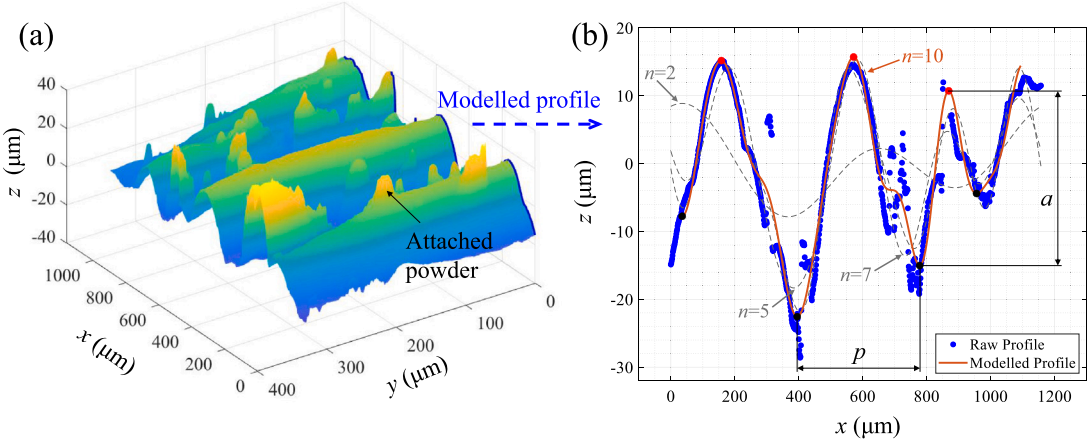

Fig. 15. (a) Surface observation of a cylindrical as-built specimen obtained with the OP and (b) selected profile with the corresponding modelling with different number of harmonics.

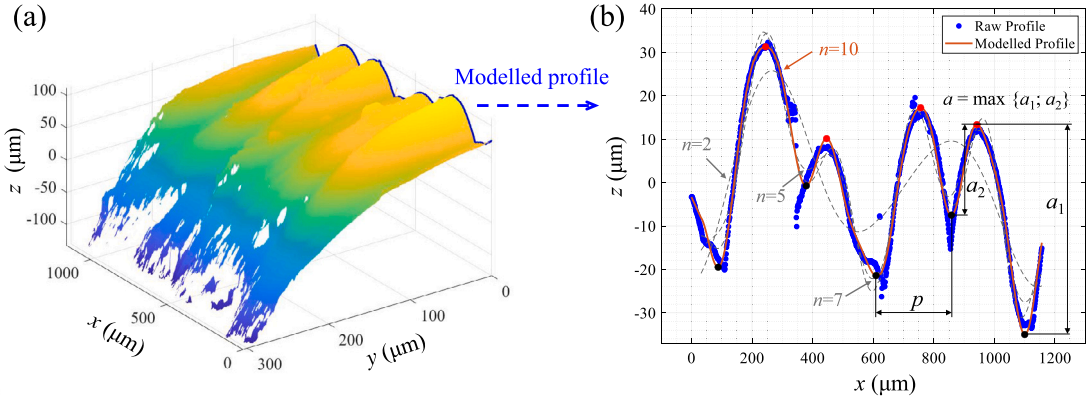

Fig. 16. (a) Surface observation of a miniaturized plain as-built specimen obtained with the OP and (b) selected profile with the corresponding modelling with different number of harmonics.

to this, the critical roughness value for the fatigue strength could be found located away from the scanned region, however, still within the HSS. Despite the absence of evident lacks of fusion or keyhole defects, as shown in Fig. 6, there is a residual possible synergistic combination between the surface roughness and the internal sporadic porosity, which is obviously probabilistic, and then dependent on the size. In order to calibrate the model, the parameters to be found were S_0 and m, and they were determined by combining the strengths of the cylindrical and the miniaturized plain specimens, both in the as-built surface condition and at the fatigue limit (2×10^6 cycles). The system of equations reported in Eq. (10) was then solved to calculate the values of S_0 and m. According to Eq. (10), the parameter S_0 can be interpreted as a reference surface to make the introduced corrective term dimensionless, while m is just the common exponent of the HSV

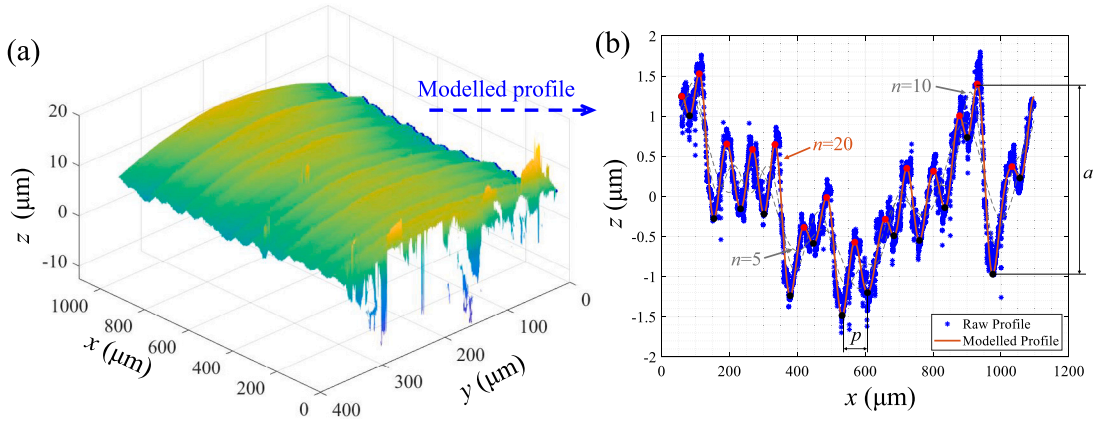

Fig. 17. (a) Surface observation of a cylindrical machined specimen obtained with the OP and (b) selected profile with the corresponding modelling with different number of harmonics.

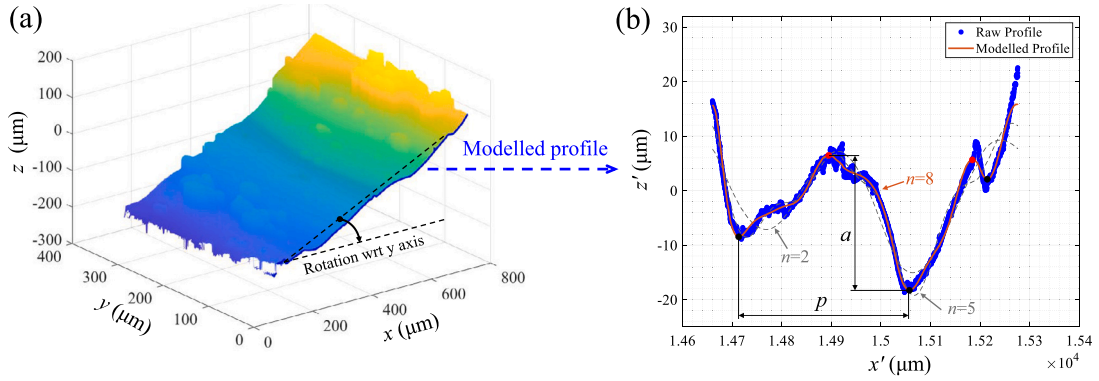

Fig. 18. (a) Surface observation of a miniaturized notched specimen obtained with the OP and (b) selected profile with the corresponding modelling with different number of harmonics.

model. The quantities $\sigma_{\text{pl, fl}}$ and $\sigma_{\text{mini, fl}}$ in Eqs. (10) correspond to the experimental fatigue limits of the cylindrical as-built and the miniaturized plain specimens, which were extracted from the fitting procedure presented in Fig. 5 at 2×10^6 cycles, thus all the quantities in Eqs. (10) are experimentally known, and then S_0 and m can be finally extracted.

$$\sigma_{\text{pl, fl}} = \frac{1.43\,(H_V+120)}{\left(\sqrt{area}_{R,1}\right)^{1/6}}\left(\frac{1-R}{2}\right)^{1/2}\left(\frac{S_0}{S_{pl}}\right)^{m}$$
$$\sigma_{\text{mini, fl}} = \frac{1.43\,(H_V+120)}{\left(\sqrt{area}_{R,2}\right)^{1/6}}\left(\frac{1-R}{2}\right)^{1/2}\left(\frac{S_0}{S_{mini}}\right)^{m} \quad (10)$$

The obtained values of S_0 and m are: S_0 = 0.105 mm^2 and m = 0.079 as reported in Table 5. At this point the machined cylindrical after turning machining and the miniaturized notched specimens were considered for a validation. By substituting the values of $\sqrt{area}_{R,3}$ and $\sqrt{area}_{R,4}$ in Eq. (9), the predicted values of the fatigue limit for the machined cylindrical specimen and for the miniaturized notched specimen were: $\sigma_{\text{pred,pl,m}}$ = 213 MPa and $\sigma_{\text{pred,mini,n}}$ = 221 MPa while the corresponding experimental values, from the S-N curve in Fig. 5, were equal to $\sigma_{\text{pl,m,fl}}$ = 205 MPa and $\sigma_{\text{mini,n,fl}}$ = 204 MPa, respectively. The prediction errors are quite low, as shown in Table 5.

The cylindrical and the miniaturized specimens fatigue strengths, and the corresponding (equivalent) defect sizes were presented on a Kitagawa–Takahashi diagram [82,83], Fig. 19. In this latter, the oblique lines indicate those according to Eq. (9) for the cylindrical and the miniaturized specimens, i.e. the 1/6 slope in log–log coordinates, while the horizontal dashed lines are the ideal values of the fatigue limit for the various specimens if perfectly smooth. In Fig. 19 the experimental values of the fatigue limit of the machined cylindrical specimen and of the miniaturized notched specimen are also reported together with the corresponding error bars, which correspond to 10% and 90% of probability of failure and they were calculated by the standard deviations of the corresponding experimental fitting curves of Fig. 5. It is highlighted that the predicted curves of the machined cylindrical specimen and of the miniaturized notched specimen are within the corresponding error bars. The fatigue limit of the ideal smooth cylindrical specimen was conservatively determined supposing that the obtained value of $\sqrt{area}_{R,3}$, for the machined cylindrical specimen, was the threshold value $\left(\sqrt{area}_{R,crit.}\right)$ for the application of a defect tolerant approach or, in other words, it was assumed that a lower surface roughness would not further increase the fatigue strength. Therefore, the corresponding stress value obtained with Eq. (9) was considered as the conservative fatigue limit of the perfectly smooth cylindrical specimen. The value of $\sqrt{area}_{R,crit.}$ was also employed to calculate the values of the fatigue limit for the miniaturized plain and notched specimens if perfectly smooth. Thus, the corresponding values of the fatigue limit for the ideal smooth miniaturized plain and miniaturized notched specimens were calculated by the application of Eq. (9) at that critical value of the equivalent defect, which is: 6.75 μm. Since the application of the proposed model in Eq. (9) to calculate the fatigue limit of the machined cylindrical specimen provided quite accurate prediction results, the actual value of $\sqrt{area}_{R,crit.}$ would be surely lower than that supposed in this research (which is the only experimentally available), thus leading to a higher value of the ideally smooth specimens fatigue limits.

Table 5
Calibration values of the proposed model parameters and numerical results of the fatigue limit prediction validations obtained with the cylindrical machined specimen and with the miniaturized notched specimen.

S_0 (mm^2)	m	Exp. $\sigma_{pl,m,fl}$ (MPa)	Pred. $\sigma_{pl,m,fl}$ (MPa)	Err. (%)	Exp. $\sigma_{mini,n,fl}$ (MPa)	Pred. $\sigma_{mini,n,fl}$ (MPa)	Err. (%)
0.105	0.079	205	213	3.9	204	221	8.3

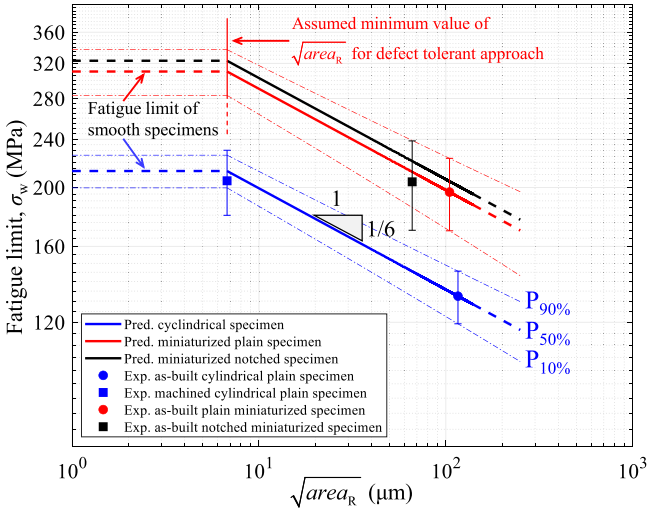

Fig. 19. Dependence of the fatigue limits of the cylindrical and the miniaturized specimens on the value of $\sqrt{area_R}$ according to the proposed model. The oblique dashed–dotted lines define the probability of failure at 90% and at 10%, and the corresponding standard deviations were extracted from the experimental fatigue tests reported in Fig. 5.

4. Conclusions

In this research the fatigue strength of cylindrical and miniaturized specimens, made of Inconel 718 and produced by L-PBF, was investigated. After the manufacturing, the specimens underwent an aging treatment, and turning machining was applied to a series of cylindrical plain specimens, to reduce the surface roughness and then investigate its role on the fatigue strength. The specimens were analysed with an optical microscope for metallographic investigations, with the SEM for fractographic analyses for a better understanding of the fatigue initiation, and by means of a 3D optical profilometer to obtain the surface topography. The surface profiles were then replicated as a sum of harmonics with the fast Fourier transform (FFT) algorithm to filter very high frequencies which could imply incorrect evaluation of the profile shape. The proposed approach combined the Murakami formula with the related roughness parameter, an additional term to account for the nonzero value of the average stress, and an additional term inspired from the HSV criterion and reformulated as highly stressed surface (HSS). This latter reformulation was introduced just considering that the fatigue failure generally initiates at the surface.

Some remarks about the obtained results are provided below:

1. Once the surface profiles of the investigated specimens were reproduced by the FFT, the couples of a and p leading to the highest value of the Murakami roughness parameter $\sqrt{area_R}$ were identified for the cylindrical plain (both as-built and machined) and the miniaturized (plain and notched) specimens. The two obtained maximum equivalent defects for the as-built cylindrical and for the miniaturized plain specimens resulted very similar, which means that the 3D printing machine was able to provide a quite repeatable surface profile regardless of the type of the printed section shape.
2. According to the previous point, it follows that Eq. (4), combined with Eq. (8), is not able to explain the experimental difference of the fatigue strength shown in Fig. 5 between the miniaturized plain and the common size specimens, despite their different dimensions. The proposed criterion, however, is able to include the modelling of the size effect through the term $(S_0/S)^m$ in Eq. (9), where S represents the HSS, which had a significantly different size between the cylindrical specimen and the miniaturized one. This latter implies a higher probability of finding either a more severe surface roughness or a combined effect of the surface roughness and any defect near the surface. These critical conditions could be found away from the analysed portion but still within the HSS.
3. The values of S_0 and m were calculated by combining the cylindrical and the miniaturized plain specimens in as-built condition, while the machined cylindrical and the miniaturized notched specimens were then used to validate the proposed model.
4. Nevertheless the term $(S_0/S)^m$ played a crucial role to account for the size effect, the most consistent part of the proposed model is the term $\sqrt{area_R}$, according to the Murakami formulation [2]. This latter statement can also be justified observing that the obtained value of m reported in Table 5 resulted close to zero.
5. As an alternative to the proposed model, even the additional term 120 in Eq. (9) could be considered as an unknown parameter, as proposed in the previous research [18]. Following this idea, the parameters to be tuned were three: the additional term, m and S_0. The as-built cylindrical, the miniaturized plain and the machined cylindrical specimens were employed to calculate the values of the parameters and the miniaturized notched specimen was used as a validator. A low prediction error was obtained, however, with no substantial differences with respect to the model proposed in this research.
6. The obtained value of $\sqrt{area_{R,3}}$, corresponding to the highest Murakami roughness parameter of the machined cylindrical specimen, was considered as the threshold $\sqrt{area_{R,crit.}}$ for the application of a defect tolerant approach, as presented in Fig. 19. By supposing the same value of $\sqrt{area_{R,crit.}}$, the fatigue limits of ideally smooth specimens (cylindrical or miniaturized) were conservatively estimated. Considering that the proposed model is a defect tolerant approach, and by employing $\sqrt{area_{R,3}}$ it provided an accurate prediction of the fatigue limit of the machined cylindrical specimen, the threshold value of $\sqrt{area_{crit.}}$ would be lower (or at least equal) than $\sqrt{area_{R,3}}$.

CRediT authorship contribution statement

Giuseppe Macoretta: Conceptualization, Data curation, Investigation, Methodology, Software, Supervision, Validation, Writing – original draft, Writing – review & editing. **Lorenzo Romanelli:** Conceptualization, Investigation, Methodology, Software, Validation, Writing – original draft, Writing – review & editing. **Ciro Santus:** Conceptualization, Investigation, Methodology, Software, Supervision, Validation, Writing – original draft, Writing – review & editing. **Luca Romoli:** Data curation, Investigation, Methodology, Supervision, Validation, Writing – review & editing. **Adrian Hugh Alexander Lutey:** Data curation, Investigation, Methodology, Software, Validation, Writing – review & editing. **Federico Uriati:** Conceptualization, Investigation, Methodology, Software, Validation, Writing – review & editing. **Gianni Nicoletto:** Conceptualization, Data curation, Investigation, Methodology,

Software, Supervision, Validation, Writing – review & editing. **Sunil Raghavendra:** Data curation, Investigation, Methodology, Software, Writing – review & editing. **Matteo Benedetti:** Conceptualization, Data curation, Investigation, Methodology, Software, Supervision, Writing – original draft, Writing – review & editing. **Bernardo Disma Monelli:** Conceptualization, Data curation, Investigation, Methodology, Software, Supervision, Writing – review & editing.

Declaration of competing interest

We wish to confirm that there are no known conflicts of interest associated with this publication and there has been no significant financial support for this work that could have influenced its outcome.

We confirm that the manuscript has been read and approved by all named authors and that there are no other persons who satisfied the criteria for authorship but are not listed. We further confirm that the order of authors listed in the manuscript has been approved by all of us.

We confirm that we have given due consideration to the protection of intellectual property associated with this work and that there are no impediments to publication, including the timing of publication, with respect to intellectual property. In so doing we confirm that we have followed the regulations of our institutions concerning intellectual property.

We understand that the Corresponding Author is the sole contact for the Editorial process (including Editorial Manager and direct communications with the office). He/she is responsible for communicating with the other authors about progress, submissions of revisions and final approval of proofs.

Data availability

The data are presented at the end of the paper.

Acknowledgements

This work was partially supported by grant PRA_2022_65 from the University of Pisa, Italy.

Appendix. Fatigue data

In this appendix all the fatigue data obtained during the fatigue tests of the four kinds of specimens involved in the research are reported.

Cylindrical as-built, $R = 0$		Miniaturized plain, $R = 0$	
Number of cycles to failure (N_f)	Stress amplitude (MPa)	Number of cycles to failure (N_f)	Stress amplitude (MPa)
5.69×10^4	315	3.70×10^4	369
7.61×10^4	316	1.33×10^5	318
1.20×10^5	261	1.48×10^5	344
1.45×10^5	261	1.55×10^5	296
1.50×10^5	261	1.79×10^5	285
2.53×10^5	214	1.92×10^5	271
2.69×10^5	214	2.02×10^5	294
4.36×10^5	190	2.07×10^5	259
4.83×10^5	214	3.08×10^5	247
8.36×10^5	166	3.46×10^5	236
9.45×10^5	166	3.86×10^5	249
9.56×10^5	152	5.09×10^5	214
1.22×10^6	145	7.93×10^5	225
1.60×10^6	140	8.13×10^5	239
2.00×10^7	140	2.00×10^6	217
2.00×10^7	128		

Cylindrical machined, $R = 0$		Miniaturized notched, $R = 0$	
Number of cycles to failure (N_f)	Stress amplitude (MPa)	Number of cycles to failure (N_f)	Stress amplitude (MPa)
1.08×10^5	321	3.98×10^4	468
1.71×10^5	321	3.99×10^4	420
1.96×10^5	285	4.67×10^4	511
2.85×10^5	285	7.26×10^4	396
5.99×10^5	238	9.60×10^4	336
6.31×10^5	238	1.41×10^5	303
6.67×10^5	226	1.41×10^5	338
7.61×10^5	209	1.68×10^5	382
7.93×10^5	202	2.16×10^5	261
8.87×10^5	202	3.29×10^5	245
1.00×10^6	226	3.46×10^5	257
1.19×10^6	238	5.16×10^5	230
2.40×10^6	202	5.63×10^5	216
2.71×10^6	214	1.00×10^6	243
4.46×10^6	202	2.00×10^6	271
		2.00×10^6	220

References

[1] Wang X, Gong X, Chou K. Review on powder-bed laser additive manufacturing of Inconel 718 parts. Proc Inst Mech Eng B 2016;231(11):1890–903. http://dx.doi.org/10.1177/0954405415619883.

[2] deBarbadillo JJ, Mannan SK. Alloy 718 for oilfield applications. JOM 2012;64(2):265–70. http://dx.doi.org/10.1007/s11837-012-0238-z.

[3] Kumar SP, Elangovan S, Mohanraj R, Ramakrishna JR. A review on properties of Inconel 625 and Inconel 718 fabricated using direct energy deposition. Mater Today: Proc 2021;46:7892–906. http://dx.doi.org/10.1016/j.matpr.2021.02.566.

[4] Cersullo N, Mardaras J, Emile P, Nickel K, Holzinger V, Hühne C. Effect of internal defects on the fatigue behavior of additive manufactured metal components: A comparison between Ti6Al4V and Inconel 718. Materials 2022;15(19):6882. http://dx.doi.org/10.3390/ma15196882.

[5] Patel S, deBarbadillo J, Coryell S. Superalloy 718: Evolution of the alloy from high to low temperature application. In: The minerals, metals & materials series. Springer International Publishing; 2018, p. 23–49. http://dx.doi.org/10.1007/978-3-319-89480-5_2.

[6] Fayed EM, Shahriari D, Saadati M, Brailovski V, Jahazi M, Medraj M. Influence of homogenization and solution treatments time on the microstructure and hardness of Inconel 718 fabricated by laser powder bed fusion process. Materials 2020;13(11):2574. http://dx.doi.org/10.3390/ma13112574.

[7] Giorgetti A, Baldi N, Palladino M, Ceccanti F, Arcidiacono G, Citti P. A method to optimize parameters development in L-PBF based on single and multitracks analysis: A case study on Inconel 718 alloy. Metals 2023;13(2):306. http://dx.doi.org/10.3390/met13020306.

[8] Hosseini E, Popovich VA. A review of mechanical properties of additively manufactured Inconel 718. Addit Manuf 2019;30:100877. http://dx.doi.org/10.1016/j.addma.2019.100877.

[9] Guo C, Li S, Shi S, Li X, Hu X, Zhu Q, Ward RM. Effect of processing parameters on surface roughness, porosity and cracking of as-built IN738LC parts fabricated by laser powder bed fusion. J Mater Process Technol 2020;285:116788. http://dx.doi.org/10.1016/j.jmatprotec.2020.116788.

[10] Liu SY, Li HQ, Qin CX, Zong R, Fang XY. The effect of energy density on texture and mechanical anisotropy in selective laser melted Inconel 718. Mater Des 2020;191:108642. http://dx.doi.org/10.1016/j.matdes.2020.108642.

[11] Balbaa M, Mekhiel S, Elbestawi M, McIsaac J. On selective laser melting of Inconel 718: Densification, surface roughness, and residual stresses. Mater Des 2020;193:108818. http://dx.doi.org/10.1016/j.matdes.2020.108818.

[12] Tucho WM, Cuvillier P, Sjolyst-Kverneland A, Hansen V. Microstructure and hardness studies of Inconel 718 manufactured by selective laser melting before and after solution heat treatment. Mater Sci Eng A 2017;689:220–32. http://dx.doi.org/10.1016/j.msea.2017.02.062.

[13] Scime L, Beuth J. Melt pool geometry and morphology variability for the Inconel 718 alloy in a laser powder bed fusion additive manufacturing process. Addit Manuf 2019;29:100830. http://dx.doi.org/10.1016/j.addma.2019.100830.

[14] Shoukr D, Morcos P, Sundermann T, Dobrowolski T, Yates C, Jain JR, Arróyave R, Karaman I, Elwany A. Influence of layer thickness on the printability of nickel alloy 718:A systematic process optimization framework. Addit Manuf 2023;73:103646. http://dx.doi.org/10.1016/j.addma.2023.103646.

[15] Rosenthal D. The theory of moving sources of heat and its application to metal treatments. J Fluids Eng 1946;68(8):849–65. http://dx.doi.org/10.1115/1.4018624.
[16] Wang Y, Lu Y, Mendez PF. Scaling expressions of characteristic values for a moving point heat source in steady state on a semi-infinite solid. Int J Heat Mass Transfer 2019;135:1118–29. http://dx.doi.org/10.1016/j.ijheatmasstransfer.2019.02.042.
[17] Moda M, Chiocca A, Macoretta G, Monelli BD, Bertini L. Technological implications of the Rosenthal solution for a moving point heat source in steady state on a semi-infinite solid. Mater Des 2022;223:110991. http://dx.doi.org/10.1016/j.matdes.2022.110991.
[18] Macoretta G, Bertini L, Monelli BD, Berto F. Productivity-oriented SLM process parameters effect on the fatigue strength of Inconel 718. Int J Fatigue 2023;168:107384. http://dx.doi.org/10.1016/j.ijfatigue.2022.107384.
[19] Yu C, Huang Z, Zhang Z, Shen J, Wang J, Xu Z. Influence of post-processing on very high cycle fatigue resistance of Inconel 718 obtained with laser powder bed fusion. Int J Fatigue 2021;153:106510. http://dx.doi.org/10.1016/j.ijfatigue.2021.106510.
[20] Zhang D, Niu W, Cao X, Liu Z. Effect of standard heat treatment on the microstructure and mechanical properties of selective laser melting manufactured Inconel 718 superalloy. Mater Sci Eng A 2015;644:32–40. http://dx.doi.org/10.1016/j.msea.2015.06.021.
[21] Solberg K, Wan D, Berto F. Fatigue assessment of as-built and heat-treated Inconel 718 specimens produced by additive manufacturing including notch effects. Fatigue Fract Eng Mater Struct 2020;43(10):2326–36. http://dx.doi.org/10.1111/ffe.13300.
[22] Witkin DB, Patel D, Albright TV, Bean GE, McLouth T. Influence of surface conditions and specimen orientation on high cycle fatigue properties of Inconel 718 prepared by laser powder bed fusion. Int J Fatigue 2020;132:105392. http://dx.doi.org/10.1016/j.ijfatigue.2019.105392.
[23] Kim S, Choi H, Lee J, Kim S. Room and elevated temperature fatigue crack propagation behavior of Inconel 718 alloy fabricated by laser powder bed fusion. Int J Fatigue 2020;140:105802. http://dx.doi.org/10.1016/j.ijfatigue.2020.105802.
[24] Uriati F, Nicoletto G, Lutey AHA. As-built surface quality and fatigue resistance of Inconel 718 obtained by additive manufacturing. Mater Des Process Commun 2021;3(4). http://dx.doi.org/10.1002/mdp2.228.
[25] Yamada Y, Newman JC. Crack closure under high load-ratio conditions for Inconel-718 near threshold behavior. Eng Fract Mech 2009;76(2):209–20. http://dx.doi.org/10.1016/j.engfracmech.2008.09.009.
[26] Klumpp A, Maier S, Chen H, Fotouhi M, Schneider R, Dietrich S, Lang K-H, Schulze V. Influence of work-hardening on fatigue crack growth, effective threshold and crack opening behavior in the nickel-based superalloy Inconel 718. Int J Fatigue 2018;116:257–67. http://dx.doi.org/10.1016/j.ijfatigue.2018.06.033.
[27] Hua Y, Liu Z. Effects of machining induced residual shear and normal stresses on fatigue life and stress intensity factor of Inconel 718. Appl Sci 2019;9(22):4750. http://dx.doi.org/10.3390/app9224750.
[28] Watring DS, Carter KC, Crouse D, Raeymaekers B, Spear AD. Mechanisms driving high-cycle fatigue life of as-built Inconel 718 processed by laser powder bed fusion. Mater Sci Eng A 2019;761:137993. http://dx.doi.org/10.1016/j.msea.2019.06.003.
[29] Yamashita Y, Murakami T, Mihara R, Okada M, Murakami Y. Defect analysis and fatigue design basis for Ni-based superalloy 718 manufactured by selective laser melting. Int J Fatigue 2018;117:485–95. http://dx.doi.org/10.1016/j.ijfatigue.2018.08.002.
[30] Dastgerdi JN, Jaberi O, Remes H, Lehto P, Toudeshky HH, Kuva J. Fatigue damage process of additively manufactured 316 L steel using X-ray computed tomography imaging. Addit Manuf 2023;70:103559. http://dx.doi.org/10.1016/j.addma.2023.103559.
[31] Foti P, Razavi N, Fatemi A, Berto F. Multiaxial fatigue of additively manufactured metallic components: A review of the failure mechanisms and fatigue life prediction methodologies. Prog Mater Sci 2023;137:101126. http://dx.doi.org/10.1016/j.pmatsci.2023.101126.
[32] Molaei R, Fatemi A, Phan N. Significance of hot isostatic pressing (HIP) on multiaxial deformation and fatigue behaviors of additive manufactured Ti-6Al-4V including build orientation and surface roughness effects. Int J Fatigue 2018;117:352–70. http://dx.doi.org/10.1016/j.ijfatigue.2018.07.035.
[33] Gates NR, Fatemi A. On the consideration of normal and shear stress interaction in multiaxial fatigue damage analysis. Int J Fatigue 2017;100:322–36. http://dx.doi.org/10.1016/j.ijfatigue.2017.03.042.
[34] Molaei R, Fatemi A, Phan N. Multiaxial fatigue of LB-PBF additive manufactured 17–4 PH stainless steel including the effects of surface roughness and HIP treatment and comparisons with the wrought alloy. Int J Fatigue 2020;137:105646. http://dx.doi.org/10.1016/j.ijfatigue.2020.105646.
[35] Fatemi A, Molaei R, Phan N. Multiaxial fatigue of additive manufactured metals: Performance, analysis, and applications. Int J Fatigue 2020;134:105479. http://dx.doi.org/10.1016/j.ijfatigue.2020.105479.
[36] Taylor D. The theory of critical distances. Eng Fract Mech 2008;75(7):1696–705. http://dx.doi.org/10.1016/j.engfracmech.2007.04.007.
[37] Santus C, Romanelli L, Grossi T, Neri P, Romoli L, Lutey AHA, Pedranz M, Benedetti M. Torsional-loaded notched specimen fatigue strength prediction based on mode I and mode III critical distances and fracture surface investigations with a 3D optical profilometer. Int J Fatigue 2022;161:106913. http://dx.doi.org/10.1016/j.ijfatigue.2022.106913.
[38] Taylor D. The theory of critical distances. Elsevier Science; 2007, p. 306. http://dx.doi.org/10.1016/B978-0-08-044478-9.X5000-5.
[39] Santus C, Taylor D, Benedetti M. Experimental determination and sensitivity analysis of the fatigue critical distance obtained with rounded V-notched specimens. Int J Fatigue 2018;113:113–25. http://dx.doi.org/10.1016/j.ijfatigue.2018.03.037.
[40] Santus C, Taylor D, Benedetti M. Determination of the fatigue critical distance according to the Line and the Point Methods with rounded V-notched specimen. Int J Fatigue 2018;106:208–18. http://dx.doi.org/10.1016/j.ijfatigue.2017.10.002.
[41] Benedetti M, Santus C, Fontanari V, Lusuardi D, Zanini F, Carmignato S. Plain and notch fatigue strength of thick-walled ductile cast iron EN-GJS-600-3: A double-notch critical distance approach to defect sensitivity. Int J Fatigue 2021;152:106414. http://dx.doi.org/10.1016/j.ijfatigue.2021.106414.
[42] Benedetti M, Santus C. Notch fatigue and crack growth resistance of Ti-6Al-4V ELI additively manufactured via selective laser melting: A critical distance approach to defect sensitivity. Int J Fatigue 2019;121:281–92. http://dx.doi.org/10.1016/j.ijfatigue.2018.12.020.
[43] Gillham B, Yankin A, McNamara F, Tomonto C, Taylor D, Lupoi R. Application of the Theory of Critical Distances to predict the effect of induced and process inherent defects for SLM Ti-6Al-4V in high cycle fatigue. CIRP Ann 2021;70(1):171–4. http://dx.doi.org/10.1016/j.cirp.2021.03.004.
[44] Benedetti M, Santus C, Raghavendra S, Lusuardi D, Zanini F, Carmignato S. Multiaxial plain and notch fatigue strength of thick-walled ductile cast iron EN-GJS-600-3: Combining multiaxial fatigue criteria, theory of critical distances, and defect sensitivity. Int J Fatigue 2022;156:106703. http://dx.doi.org/10.1016/j.ijfatigue.2021.106703.
[45] Beretta S, Romano S. A comparison of fatigue strength sensitivity to defects for materials manufactured by AM or traditional processes. Int J Fatigue 2017;94:178–91. http://dx.doi.org/10.1016/j.ijfatigue.2016.06.020.
[46] Zhang J, Fatemi A. Surface roughness effect on multiaxial fatigue behavior of additive manufactured metals and its modeling. Theor Appl Fract Mech 2019;103:102260. http://dx.doi.org/10.1016/j.tafmec.2019.102260.
[47] Molaei R, Fatemi A. Fatigue performance of additive manufactured metals under variable amplitude service loading conditions including multiaxial stresses and notch effects: Experiments and modelling. Int J Fatigue 2021;145:106002. http://dx.doi.org/10.1016/j.ijfatigue.2020.106002.
[48] Molaei R, Fatemi A, Phan N. Notched fatigue of additive manufactured metals under axial and multiaxial loadings, part II: Data correlations and life estimations. Int J Fatigue 2022;156:106648. http://dx.doi.org/10.1016/j.ijfatigue.2021.106648.
[49] Molaei R, Fatemi A, Sanaei N, Pegues J, Shamsaei N, Shao S, Li P, Warner DH, Phan N. Fatigue of additive manufactured Ti-6Al-4V, Part II: The relationship between microstructure, material cyclic properties, and component performance. Int J Fatigue 2020;132:105363. http://dx.doi.org/10.1016/j.ijfatigue.2019.105363.
[50] Pugno N, Ciavarella M, Cornetti P, Carpinteri A. A generalized Paris' law for fatigue crack growth. J Mech Phys Solids 2006;54(7):1333–49. http://dx.doi.org/10.1016/j.jmps.2006.01.007.
[51] Sanaei N, Fatemi A. Defect-based multiaxial fatigue life prediction of L-PBF additive manufactured metals. Fatigue Fract Eng Mater Struct 2021;44(7):1897–915. http://dx.doi.org/10.1111/ffe.13449.
[52] Murakami Y. Material defects as the basis of fatigue design. Int J Fatigue 2012;41:2–10. http://dx.doi.org/10.1016/j.ijfatigue.2011.12.001.
[53] Fatemi A, Molaei R, Sharifimehr S, Shamsaei N, Phan N. Torsional fatigue behavior of wrought and additive manufactured Ti-6Al-4V by powder bed fusion including surface finish effect. Int J Fatigue 2017;99:187–201. http://dx.doi.org/10.1016/j.ijfatigue.2017.03.002.
[54] Fatemi A, Molaei R, Sharifimehr S, Phan N, Shamsaei N. Multiaxial fatigue behavior of wrought and additive manufactured Ti-6Al-4V including surface finish effect. Int J Fatigue 2017;100:347–66. http://dx.doi.org/10.1016/j.ijfatigue.2017.03.044.
[55] Masuo H, Tanaka Y, Morokoshi S, Yagura H, Uchida T, Yamamoto Y, Murakami Y. Influence of defects, surface roughness and HIP on the fatigue strength of Ti-6Al-4V manufactured by additive manufacturing. Int J Fatigue 2018;117:163–79. http://dx.doi.org/10.1016/j.ijfatigue.2018.07.020.
[56] Ma XF, Zhai HL, Zuo L, Zhang WJ, Rui SS, Han QN, Jiang JS, Li CP, Chen GF, Qian GA, Zhao SJ. Fatigue short crack propagation behavior of selective laser melted Inconel 718 alloy by in-situ SEM study: Influence of orientation and temperature. Int J Fatigue 2020;139:105739. http://dx.doi.org/10.1016/j.ijfatigue.2020.105739.
[57] Uriati F, Nicoletto G. A comparison of Inconel 718 obtained with three L-PBF production systems in terms of process parameters, as-built surface quality, and fatigue performance. Int J Fatigue 2022;162:107004. http://dx.doi.org/10.1016/j.ijfatigue.2022.107004.

[58] Nicoletto G. Smooth and notch fatigue behavior of selectively laser melted Inconel 718 with as-built surfaces. Int J Fatigue 2019;128:105211. http://dx.doi.org/10.1016/j.ijfatigue.2019.105211.
[59] Nicoletto G, Tinelli G, Lutey AHA, Romoli L. Influence of as-built surface topography on the fatigue behavior of SLM Inconel 718 : experiments and modeling. In: Sim-AM 2019 : II international conference on simulation for additive manufacturing. 2019.
[60] Macek W, Nejad RM, Zhu S-P, Trembacz J, Branco R, Costa JDM, Fereira JAM, Capela C. Effect of bending-torsion on fracture and fatigue life for 18Ni300 steel specimens produced by SLM. Mech Mater 2023;178:104576. http://dx.doi.org/10.1016/j.mechmat.2023.104576.
[61] Macek W, Tomczyk A, Branco R, Dobrzyński M, Seweryn A. Fractographical quantitative analysis of EN-AW 2024 aluminum alloy after creep pre-strain and LCF loading. Eng Fract Mech 2023;282:109182. http://dx.doi.org/10.1016/j.engfracmech.2023.109182.
[62] Macek W, Rozumek D, Faszynka S, Branco R, Zhu S-P, Nejad RM. Fractographic-fractal dimension correlation with crack initiation and fatigue life for notched aluminium alloys under bending load. Eng Fail Anal 2023;149:107285. http://dx.doi.org/10.1016/j.engfailanal.2023.107285.
[63] Macek W, Branco R, Podulka P, Nejad RM, Costa JD, Ferreira JAM, Capela C. The correlation of fractal dimension to fracture surface slope for fatigue crack initiation analysis under bending-torsion loading in high-strength steels. Measurement 2023;218:113169. http://dx.doi.org/10.1016/j.measurement.2023.113169.
[64] Murakami Y. Metal fatigue. Elsevier; 2019, http://dx.doi.org/10.1016/c2016-0-05272-5.
[65] Barros R, Silva FJG, Gouveia RM, Saboori A, Marchese G, Biamino S, Salmi A, Atzeni E. Laser powder bed fusion of Inconel 718: Residual stress analysis before and after heat treatment. Metals 2019;9(12):1290. http://dx.doi.org/10.3390/met9121290.
[66] Marchese G, Atzeni E, Salmi A, Biamino S. Microstructure and residual stress evolution of laser powder bed fused Inconel 718 under heat treatments. J Mater Eng Perform 2020;30(1):565–74. http://dx.doi.org/10.1007/s11665-020-05338-z.
[67] Nicoletto G. A novel test method for the fatigue characterization of metal powder bed fused alloys. Procedia Struct Integr 2017;7:67–74. http://dx.doi.org/10.1016/j.prostr.2017.11.062.
[68] Wang R, Chen C, Liu M, Zhao R, Xu S, Hu T, Shuai S, Liao H, Ke L, Vanmeensel K, Wang J, Ren Z. Effects of laser scanning speed and building direction on the microstructure and mechanical properties of selective laser melted Inconel 718 superalloy. Mater Today Commun 2022;30:103095. http://dx.doi.org/10.1016/j.mtcomm.2021.103095.
[69] Ghorbanpour S, Deshmukh K, Sahu S, Riemslag T, Reinton E, Borisov E, Popovich A, Bertolo V, Jiang Q, Sanchez MT, Knezevic M, Popovich V. Additive manufacturing of functionally graded inconel 718: Effect of heat treatment and building orientation on microstructure and fatigue behaviour. J Mater Process Technol 2022;306:117573. http://dx.doi.org/10.1016/j.jmatprotec.2022.117573.
[70] Santus C, Romanelli L, Grossi T, Bertini L, Bone LL, Chiesi F, Tognarelli L. Elastic–plastic analysis of high load ratio fatigue tests on a shot-peened quenched and tempered steel, combining the Chaboche model and the Theory of Critical Distances. Int J Fatigue 2023;174:107713. http://dx.doi.org/10.1016/j.ijfatigue.2023.107713.
[71] Murakami Y, Keer LM. Stress intensity factors handbook, vol. 3. J Appl Mech 1993;60(4):1063. http://dx.doi.org/10.1115/1.2900983, arXiv:https://asmedigitalcollection.asme.org/appliedmechanics/article-pdf/60/4/1063/5463111/1063_1.pdf.
[72] Kuguel R. A relation between theoretical stress concentration factor and fatigue notch factor deduced from the concept of highly stressed volume. In: Proc. ASTM, Vol. 61. 1961, p. 732–48.
[73] Heckel K, Köhler J, München T. Experimentelle untersuchung des statistischen größeneinflusses im dauerschwingversuch an ungekerbten stahlproben. Materwiss Werksttech 1975;6(2):52–4. http://dx.doi.org/10.1002/mawe.19750060204.
[74] Böhm J, Heckel K. Die vorhersage der dauerschwingfestigkeit unter berücksichtigung des statistischen größeneinflusses. Materwiss Werksttech 1982;13(4):120–8. http://dx.doi.org/10.1002/mawe.19820130408.
[75] Ai Y, Zhu S-P, Liao D, Correia JAFO, Jesus AMPD, Keshtegar B. Probabilistic modelling of notch fatigue and size effect of components using highly stressed volume approach. Int J Fatigue 2019;127:110–9. http://dx.doi.org/10.1016/j.ijfatigue.2019.06.002.
[76] He J-C, Zhu S-P, Taddesse AT, Niu X. Evaluation of critical distance, highly stressed volume, and weakest-link methods in notch fatigue analysis. Int J Fatigue 2022;162:106950. http://dx.doi.org/10.1016/j.ijfatigue.2022.106950.
[77] Wang R, Li D, Hu D, Meng F, Liu H, Ma Q. A combined critical distance and highly-stressed-volume model to evaluate the statistical size effect of the stress concentrator on low cycle fatigue of TA19 plate. Int J Fatigue 2017;95:8–17. http://dx.doi.org/10.1016/j.ijfatigue.2016.10.003.
[78] Sonsino CM, Kaufmann H, Grubisic V. Übertragbarkeit von werkstoffkennwerten am beispiel eines betriebsfest auszulegenden geschmiedeten nutzfahrzeug-achsschenkels. 1995.
[79] Härkegård G, Halleraker G. Assessment of methods for prediction of notch and size effects at the fatigue limit based on test data by Böhm and Magin. Int J Fatigue 2010;32(10):1701–9. http://dx.doi.org/10.1016/j.ijfatigue.2010.03.011.
[80] Schumacher J, Clausen B. Calculation of the fatigue limit of high-strength steel specimens at different loading conditions based on inclusion sizes. Steel Res Int 2021;92(12). http://dx.doi.org/10.1002/srin.202100252.
[81] Pedranz M, Fontanari V, Raghavendra S, Santus C, Zanini F, Carmignato S, Lusuardi D, Berto F, Benedetti M. A new energy based highly stressed volume concept to investigate the notch-pores interaction in thick-walled ductile cast iron subjected to uniaxial fatigue. Int J Fatigue 2023;169:107491. http://dx.doi.org/10.1016/j.ijfatigue.2022.107491.
[82] Kitagawa H, Takahashi S. Applicability of fracture mechanics to very small cracks or the cracks in the early stage. In: Proc. 2nd int. conf. on mechanical behaviour of materials. 1976, p. 627–31.
[83] Benedetti M, Santus C. Building the Kitagawa-Takahashi diagram of flawed materials and components using an optimized V-notched cylindrical specimen. Eng Fract Mech 2020;224:106810. http://dx.doi.org/10.1016/j.engfracmech.2019.106810.